HIGH-THROUGHPUT SCREENING FOR NOVEL PROTON CONDUCTORS

by

Pandu Wisesa

A dissertation submitted to The Johns Hopkins University in conformity with the requirements for the degree of Doctor of Philosophy.

Baltimore, Maryland
February, 2019

Abstract

Solid Oxide Fuel Cells (SOFCs) convert chemical energy to electrical energy very efficiently compared to systems that require mechanical processes. However, SOFCs require high operating temperature in the range of 650ºC – 1,000ºC which limits the environments where they can be used. Switching the diffusing ion from oxygen to hydrogen could potentially halve the operating temperature into the range of 400ºC – 800ºC. This system is what is known as Proton Conducting Solid Oxide Fuel Cell (PC-SOFC). Despite this prospect, three decades since the discovery of proton conduction in solids, we still do not have a mainstream system that takes advantage of proton conduction to generate electricity. The main obstacle to engineer this system lies with the material used as the solid electrolyte. With the rise of computing power and number of publicly available materials dataset, we aim to find an alternative material to solve this problem.

Along the way, we acknowledged that a significant number of quantum mechanical calculations would need to be done to train and verify our methods. We took this opportunity to enhance the grids used to evaluate Brillouin zone integration which would directly impact the calculation cost. This was done by creating a database of pre-calculated grids which was made through an exhaustive search for every specified grid density. This database was then benchmarked on 102 randomly-selected materials. We found that for well-converged calculations, the grids generated through the database have less than half as many symmetrically irreducible *k*-points as the

conventionally generated Monkhorst-Pack grids. This means these calculations would require less than half the time to complete for the same level of accuracy.

On searching for alternative proton conductors, we began by limiting our criteria to proton mobility and identifying the activation energy for proton diffusion as the descriptor. The entire ICSD database was filtered for oxides and then categorized by space group and structure type. We then selected a total of 51 samples from the cubic perovskite, hexagonal perovskite, spinel, and elpasolite structure types along with several other randomly selected oxides as training data. These training data was generated using a combination of Density Functional Theory (DFT) calculation and Nudged Elastic Band (NEB) method.

An energy model based on the bond-valence method and the screening Coulomb interaction was made and fitted to the training data. In analyzing the data, we found that each structure type has noise which would be minimized when the average is taken over the structure type. The difference between the training data and energy results for the structure types mentioned above were below 0.05 eV, where 0.1 eV is the accuracy for activation energy approximation using the NEB method.

Finally, we screened all the oxide structures from the ICSD database that has more than 20 members. Based on the ranking of proton mobility, we identified $CrVO_4$ orthorhombic structure type as a novel alternative to the cubic perovskite. We verified this result by running DFT calculations and NEB method on 6 members of the $CrVO_4$ structure type and found that the average difference for this structure type was 0.07 eV.

Thesis Advisor: Professor Tim Mueller

Thesis Reader: Professor Paulette Clancy

Thesis Committee:

- Professor Paulette Clancy
- Professor En Ma
- Professor Tim Mueller
- Professor Sara Thoi
- Professor A. Shoji Hall

Acknowledgement

The author would like to begin by acknowledging the funding that made these projects possible. The proton conduction project was funded by the Office of Naval Research under award ONR N00014-15-1-2494 and the *k*-points database project was funded by the National Science Foundation under award DMR-1352373.

The author would like to acknowledge all mentors he has had over the course of his life so far. The author would not have reached this point without their support and guidance. While there are many to list, the author would like to chronologically name a few which the author believes to have had the most impact. Starting from Mr. Ignatius Purwanto, the teacher that spurred the author’s interest and confidence in science, which eventually led the author to pursue a degree in Materials Science and Engineering. While working on his Bachelor’s degree, the author was especially grateful for the guidance of Dr. Ahmad Islam for introducing him to the perspectives in research and Dr. Henry Wu for teaching him the foundations of computational materials science. In parallel, the author would like to express his gratitude towards Prof. Dallas Trinkle and Prof. John Rogers for giving him opportunities to do research in their group. In addition, the author would also like to thank Prof. Mohamed Aboukhatwa for guiding him towards graduate studies.

As a graduate student, the author would like to acknowledge and be very thankful for his Ph.D. thesis advisor Prof. Tim Mueller for his trust, patience, and guidance over the author’s graduate student career. Prof. Tim Mueller has given the author a place to grow and develop skills in research and beyond. While the significant increase computing skills and materials science knowledge are a given, the author also improved his teaching, public speaking, and various other skills which are essential in life. For that, the author believes he has grown a lot as not just a researcher, but also a person due to Prof. Tim Mueller's guidance.

The author would like to thank his thesis committee members: Prof. Paulette Clancy, Prof. Jonah Erlebacher, Prof. Jeffrey Gray, Prof. Shoji Hall, Prof. E Ma, Prof. Tim Mueller, and Prof. Sara Thoi for their service and time.

The author would like to express his appreciation to the members of the Department of Materials Science and Engineering at Johns Hopkins University. Starting from current and former fellow group members, especially Dr. André Bothelo, Dr. Liang Cao, Dr. Fenglin Yuan, Kyle McGill, Alberto Hernandez-Valle, Chenyang Li, Peter Lile, Chuhong Wang, and Yunzhe Wang. The author enjoyed and will miss the comfortable atmosphere and lively discussions with fellow group members. The author would also especially like to thank the late Prof. Robert Cammarata for reinvigorating his interest in thermodynamics. In addition, the author would like to acknowledge Prof. Michael Falk for his guidance in teaching and class-building. The author would like to express his gratitude towards the admins of the department, especially Jeanine Majewski for all her support to the author from the day of the orientation until the last day of his graduate student career.

Finally, the author would like to thank his family: his parents for trusting him and letting him pursue whatever he wanted and his brother for his constant support. In addition, his friends at home and at many different cities who always welcomed him warmly and made time for him.

Dedication

My loved ones, who accepted me for who I am.

Table of Contents

List of Tables

List of Figures

1. INTRODUCTION

1.1 Progress in proton conductor research

Since its discovery in 1971 by Iwahara et al.[1, 2] , bringing the potential of proton conduction in solids to the mainstream market has been a very tantalizing goal[3]. The main reason being various applications that make use of diffusion of ions through solids, such as fuel cells, are greatly affected by the size of the diffuser. Protons have a radius that is a fraction of an oxygen ion, which it might be an alternative of. This means the mobility of protons could be much higher than oxygen ions[4, 5].

As mentioned above, one possible application for proton conductors is as a fuel cell component. Compared to systems that converts mechanical or thermal energy to electricity, the conversion from chemical energy directly to electrical energy is very efficient, in addition to be environmentally friendly[4, 6-8]. Solid oxide fuel cells (SOFCs) are among the most efficient types of fuel cells. As shown in Figure 1.1, SOFCs work by having oxygen ions diffuse through the cell, reacting with hydrogen gas in the anode and producing electricity. However, it runs at a relatively high temperature range (650ºC – 1,000ºC)[4, 5, 8-14].

Utilizing proton conductors as an electrolyte could allow the creation of a highly efficient solid oxide fuel cell that runs at relatively low temperatures. This type of fuel cell is what is known as proton conducting solid oxide fuel cell (PC-SOFC). In addition to possibly lower range of operating temperature (400ºC – 800ºC), there are other benefits such as having the reaction on the cathode which prevents the waste water from mixing with any excess fuel.[1, 3-5, 7, 8, 10-21] This comparison and the advantages PC-SOFC could bring is shown in Figure 1.1. However, over four decades since its initial discovery, the field has not moved to a commercialization phase[3].

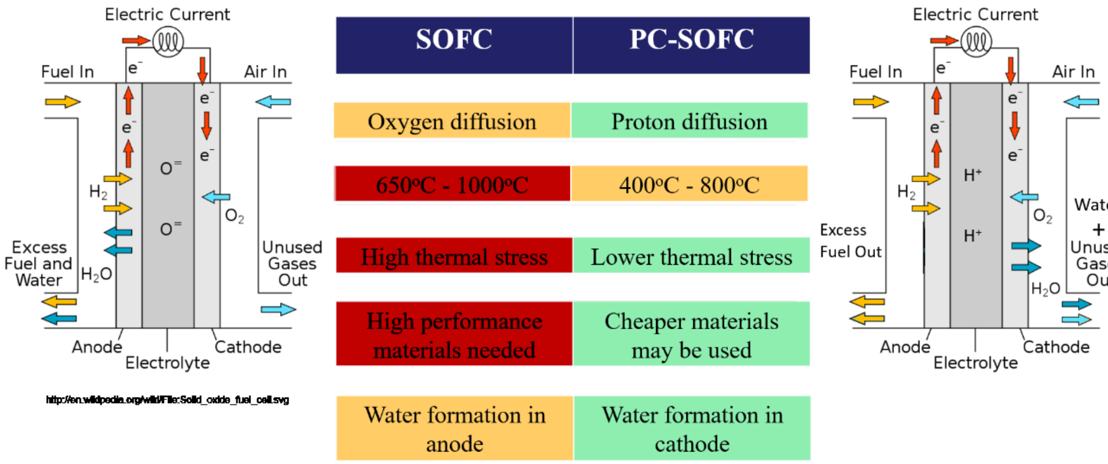

http://en.wikipedia.org/wiki/File:Solid_oxide_fuel_cell.svg

SOFC	PC-SOFC
Oxygen diffusion	Proton diffusion
650°C - 1000°C	400°C - 800°C
High thermal stress	Lower thermal stress
High performance materials needed	Cheaper materials may be used
Water formation in anode	Water formation in cathode

Figure 1.1 The mechanism of SOFC in contrast to PC-SOFC. SOFC and its traits are shown on the left. PC-SOFC and its traits are shown on the right.

Solid oxides are the most extensively studied solids for proton conductivity[3, 12, 14, 17, 22-24]. However, despite having tens of thousands of oxides in various databases, the study of proton conductivity has mainly focused on perovskites[12, 15, 17, 22, 23]. This is mainly caused by the fact that perovskites were the first structure type that was found to exhibit proton conductivity. In addition, the high symmetry in cubic perovskites lead to 3-dimensional diffusion which means that there are more possible pathways for proton to go through and to top it off, they also tend to have good proton solubility[11].

Currently the best proton conductors are the perovskite $BaZrO_3$, $BaCeO_3$, their doped variants, and combinations[3, 12, 17, 25]. However, the high conductivity of protons in $BaZrO_3$ is limited to single crystals as grain boundaries will significantly impact its overall conductivity[3, 17, 26-29]. $BaCeO_3$ and its doped variants showed promise, but at operating temperature it becomes unstable when exposed to carbon dioxide[3, 12, 17, 26, 30].

Fortunately, these challenges came at a time when computing power is large and continue to rise year after year, as shown in Figure 1.2. As described in the review paper by Curtarolo et al., there have been many examples of designing materials to solve engineering problems in the past decade[31]. From photovoltaic cells[32], to carbon capture[33], to piezoelectric material[34], to catalysts[35], and batteries[36]. By utilizing computational methods and the increasing computational powers, we could reserve the synthesis and experimental testing for materials that possess a potential to be a good proton conductor[31, 37].

Figure 1.2 A plot of high-performance computing (HPC) power with respect to time. Green circles represent the sum of the performance from the top 500 HPC, gold triangle represent the performance of the top HPC for a given year, and blue square represent the HPC on the bottom of the list. The lines represent the trends. Do note that the computing power is on a logarithmic scale[38]. Figure adapted from ref. 38.

1.2 Energy model and database screening done in this thesis

Diffusion events are kinetic processes whose transition rates are orders of magnitudes lower than the vibrations of atoms in solids. Typically, we are interested in the specific process in which the particle of interest has energy higher than the diffusion barrier and moved passed it because then we can approximate the activation energy of the diffusion process. Statistically speaking, this is a very rare event. This means directly simulating this process with quantum mechanical methods is often too costly. To overcome it, we turned to the transition state theory (TST)[39, 40]. TST relies on two assumptions, namely the transition rate is slow enough for Boltzmann distribution to be established and there is a dividing surface with lower dimensionality than the degrees of freedom of the process which represents the bottleneck. As this process cannot be directly calculated with a first principles calculation, such as Density Functional Theory (DFT)[41, 42]. It is very common to couple DFT with a method to calculate transition state properties such as the Nudged Elastic Band (NEB)[43-46] method. However, the cost of these calculations numbers in the tens of thousands of CPU hours per structure calculated and so they are not suited to screen databases.

As the interactions between hydrogen and oxide is ionic, we turned to the bond-valence (BV)[47-50] method. The BV method relates the valence of a bond to its distance. This method is originally used to estimate the oxidation states of atoms and is well parameterized for many different elements in the periodic table, making it suitable for this purpose[51]. However, on its own, the BV method does not have any energy values associated to it[51, 52]. In order to incorporate the BV method with an energy term, we coupled it with a pair potential in the form of an exponential repulsion. This term is combined with a Coulomb term to take into account the electrostatic interaction that occurs in the solid. The details of this method are explained in Chapter 3.

Ionic diffusion tends to behave similarly for a given structure type. Materials with the same structure type would share the same positions of the cations and anions, this leads them to have the same ionic diffusion channel and dimensionality. This tendency has been observed quite well in lithium[53] and was utilized to design better lithium conductors[54]. Utilizing this concept, we will also try to focus on discerning which structure types hold the potential to be a good proton conductor.

We would also like to note that the first principal calculations and BV model approaches only check the viability of a material for proton conductor based on the hydrogen mobility. Hydrogen solubility, which is another important aspect for a proton conductor is not being considered through this method.

Using the BV method to screen a database has been done with a good degree of success in lithium. Adams *et al.* connected the BV mismatch to create a potential model using a Morse-type potential and predicted various lithium ion interaction in an oxide[52, 55, 56]. Expanding on the work by Adams *et al.,* Xiao *et al.* combined said interaction potential with DFT calculations coupled with NEB method[37]. Their main reason for doing this is because even though the diffusion pathways generated by the BV-based potential model is quite accurate and the activation energy values follow the trend from the DFT coupled with NEB method values, the activation energies values are off by approximately 1eV. While this value is quite large, the main goal of their project was not to predict the exact value of the activation energy, but to get the correct "trend" in activation energy prediction and minimum energy pathways[37]. This is a conclusion we will be keeping in mind as we will be utilizing a similar approach.

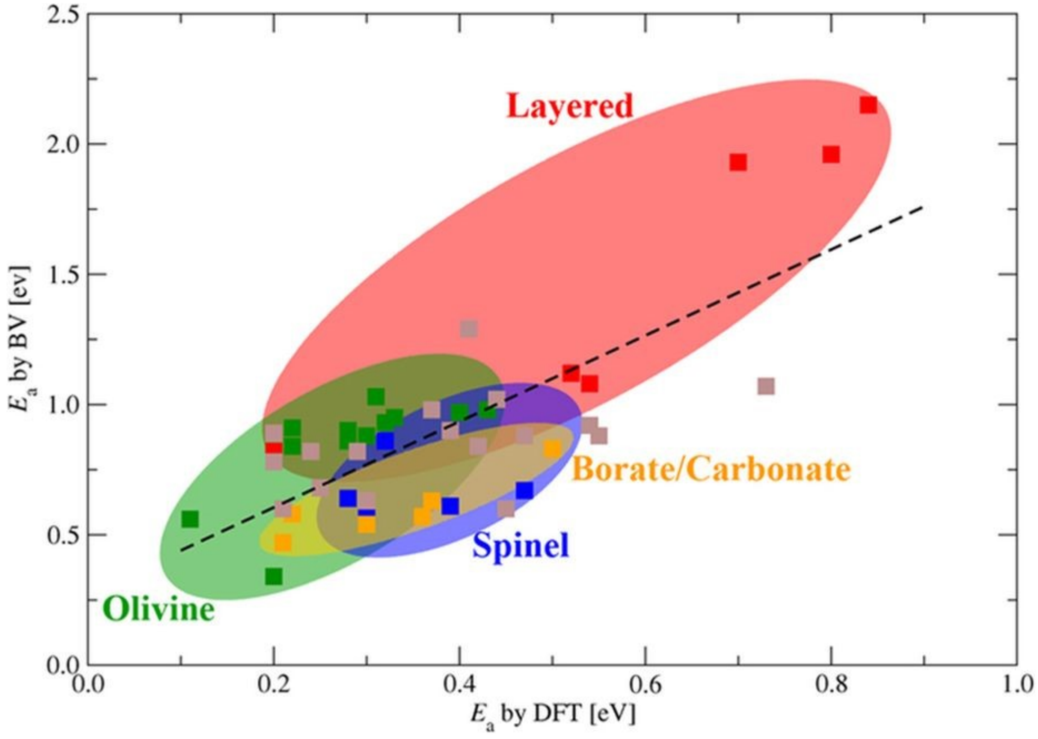

Figure 1.3. The data symbol with red, green and blue color represents the compounds in layered-, olivine- and spinel-structure, respectively. The orange symbol represents the borate and carbonate, and the brown symbol displays the results for other types including phosphate, sulphate and various structures. The dash line is a linear fit for all the data here.[37]. Figure adapted from ref. 37.

1.3 Progress in the selection of grids in sampling Brillouin zone

In computational materials science and solid-state physics, quantum mechanical methods are considered as general tools to calculate material properties. The usage of these methods often involves evaluation of integrals over the Brillouin zone in reciprocal space. These integrals are typically approximated by a discrete set of points, commonly known as *k*-points. Since these points are evaluated on the Brillouin zone of the crystal of a solid, the discrete points can be reduced by symmetry, such that no two points are symmetrically equivalent. These reduced points are what is called symmetrically irreducible *k*-points. As calculating the value at each discrete point involves solving the quantum mechanical equation once, the cost of the calculation then is linearly proportional to the number symmetrically irreducible *k*-points. Similarly, the integral approximation will become more accurate as more *k*-points in total cover the Brillouin zone evenly, as such the accuracy would also increase according to the number of points.

Several methods have been developed in order to minimize the cost while maintaining accuracy. These methods began from the concept of "special" points for Brillouin zone integration introduced by Balderschi[57] in 1973. This idea was then expanded by Chadi and Cohen[58] in the same year and was refined by Monkhorst and Pack[59] in 1976. Presently, the most commonly used method to generate grids is the one by Monkhorst and Pack.

With the rise of many computational effort in either creating or screening materials databases, we can see that any improvements to these grid generating methods would save an enormous amount of resources as it would linearly reduce computational cost.

1.4 Efficient Monkhorst-Pack grid generation method developed in this thesis

As mentioned in the chapter above, reducing computational cost while maintaining accuracy of the calculation is a very desirable prospect. There have been efforts to create a more generalized Monkhorst-Pack grids, which was first identified by Froyen[60]. This idea was later partially implemented by Moreno and Soler[61] into the SIESTA software package[62]. However, this search for the most efficient grid then involves looking through every possible grid under the user specified grid density which, depending on the given parameter, might end up costing more resources than the actual quantum mechanical calculation itself. This approach then ended up not being as popular as using a Monkhorst-Pack grid that is generated regularly along the dimensional axes.

Looking back to the discussions in the Chapter 1.1, we can see that there are currently many computational efforts, including the one discussed in this thesis, where even a small percentage of savings would translate into a large amount of CPU hours. It is then very beneficial to find a way to be able to generate a generalized Monkhorst-Pack grid while bypassing the costly search for it.

Our solution to this was to pre-generate the data seeing as there are a finite number of varieties of grids that could be used given that they have to follow the symmetry of the material in question. Once the data on the grids has been generated, we then had to tackle methods to generate, store, and use the data in a rapid and efficient manner[63]. The details to this discussion are further expanded in Chapter 2.

1.5 Scope of this thesis

This thesis covers the work that I have done as a graduate student with the guidance of my PI. It contains two different, but related projects, one on the generalized Monkhorst-Pack grid and the other on the screening for proton conductors. Chapter 2 contains the entirety of the generalized Monkhorst-Pack grid project as published in Phys. Rev. B 93 155109 (2016). Utilizing the work from Chapter 2, Chapter 3 contains the database screening for proton conductors, which has not been published yet. As mentioned in Chapter 1, the screening done in this project is limited to proton mobility and does not cover the proton solubility. In Chapter 4, I will discuss the overall conclusion of both projects along with possible future work which may be done in relation to the research that I have done.

2. EFFICIENT GENERATION OF GENERALIZED MONKHORST-PACK GRIDS THROUGH THE USE OF INFORMATICS

2.1 Introduction to generalized Monkhorst-Pack grids

As mentioned in the previous chapter, the Monkhorst-Pack grid is the most widely used grid generating method for quantum mechanical calculation. Using this method, the integral of the function is approximated by averaging the value over the *k*-points from a grid that is generated along the dimensional axes starting from the center of the Brillouin zone, or what is known as Γ point. By shifting the grid from this high-symmetry Γ point, the speed and accuracy of the approximation can be improved. The following explanation on the generalized Monkhorst-Pack grid is taken directly from our paper[63]. The axes of the grid align with the reciprocal lattice vectors, so the coordinates of a *k*-point on an $m_1 \times m_2 \times m_3$ grid are given by:

$$\mathbf{k} = \frac{n_1}{m_1}\mathbf{b}_1 + \frac{n_2}{m_2}\mathbf{b}_2 + \frac{n_3}{m_3}\mathbf{b}_3 + \mathbf{s} \tag{2.1}$$

where $\mathbf{s}$ is a vector representing the shift from the Γ point and n_1, n_2, and n_3 are integers that range from 1 to m_1, m_2, and m_3 respectively. The reciprocal lattice vectors, $\mathbf{b}_1$, $\mathbf{b}_2$ and $\mathbf{b}_3$, are defined by:

$$\begin{pmatrix}\mathbf{b}_1 & \mathbf{b}_2 & \mathbf{b}_3\end{pmatrix}^T = 2\pi\begin{pmatrix}\mathbf{a}_1 & \mathbf{a}_2 & \mathbf{a}_3\end{pmatrix}^{-1} \tag{2.2}$$

where $\mathbf{a}_1$, $\mathbf{a}_2$ and $\mathbf{a}_3$ are the lattice vectors for a primitive unit cell in real space.

Monkhorst-Pack grids have a useful real-space interpretation. We can define an $m_1 \times m_2 \times m_3$ supercell of the primitive cell with lattice vectors $\mathbf{c}_1$, $\mathbf{c}_2$, and $\mathbf{c}_3$ given by

$$\begin{pmatrix}\mathbf{c}_1 & \mathbf{c}_2 & \mathbf{c}_3\end{pmatrix} = \begin{pmatrix}\mathbf{a}_1 & \mathbf{a}_2 & \mathbf{a}_3\end{pmatrix}\mathbf{M} \tag{2.3}$$

where $\mathbf{M}$ is a diagonal matrix in which $M_{11} = m_1$, $M_{22} = m_2$, and $M_{33} = m_3$. We will refer to the Bravais lattice with lattice vectors $\mathbf{c}_1$, $\mathbf{c}_2$, and $\mathbf{c}_3$ as the "superlattice". Bloch waves with wave vector $\mathbf{s}$ with respect to the supercell take the form:

$$\psi(\mathbf{r}) = u_{\text{super}}(\mathbf{r})e^{i\mathbf{s}\cdot\mathbf{r}} \tag{2.4}$$

where $u_{\text{super}}(\mathbf{r})$ is a function with the periodicity of the real-space supercell. We can express $u_{\text{super}}(\mathbf{r})$ as a Bloch wave with respect to the *primitive* cell:

$$u_{\text{super}}(\mathbf{r}) = u_{\text{primitive}}(\mathbf{r})e^{i\mathbf{g}\cdot\mathbf{r}} \tag{2.5}$$

where $u_{\text{primitive}}(\mathbf{r})$ is a function with the periodicity of the real-space primitive cell and $\mathbf{g}$ is a vector in reciprocal space. Because $u_{\text{super}}(\mathbf{r})$ has the periodicity of the real-space supercell, $\mathbf{g}$ must satisfy

$$\mathbf{g}^{\mathbf{T}}\begin{pmatrix}\mathbf{c}_1 & \mathbf{c}_2 & \mathbf{c}_3\end{pmatrix} = 2\pi\begin{pmatrix}n_1 & n_2 & n_3\end{pmatrix} \tag{2.6}$$

where n_1, n_2, and n_3 are integers. Combining equations (3.3) and (3.6), we get:

$$\mathbf{g}^{\mathbf{T}}\begin{pmatrix}\mathbf{a}_1 & \mathbf{a}_2 & \mathbf{a}_3\end{pmatrix}\mathbf{M} = 2\pi\begin{pmatrix}n_1 & n_2 & n_3\end{pmatrix}. \tag{2.7}$$

Solving for $\mathbf{g}$ and combining with equation (2.2) yields

$$\mathbf{g}^{\mathbf{T}} = \begin{pmatrix} n_1 & n_2 & n_3 \end{pmatrix} \mathbf{M}^{-1} \begin{pmatrix} \mathbf{b}_1 & \mathbf{b}_2 & \mathbf{b}_3 \end{pmatrix}^{\mathbf{T}} . \tag{2.8}$$

Combining equations (2.4), (2.5), and (2.8), we get an alternative expression for $\psi(\mathbf{r})$:

$$\psi(\mathbf{r}) = u_{\text{primitive}}(\mathbf{r}) e^{i\left(\frac{n_1}{m_1}\mathbf{b}_1 + \frac{n_2}{m_2}\mathbf{b}_2 + \frac{n_3}{m_3}\mathbf{b}_3 + \mathbf{s}\right)\cdot\mathbf{r}} . \tag{2.9}$$

Equations (2.1), (2.4), and (2.9) demonstrate that each Bloch wave on a Monkhorst-Pack grid with respect to the primitive cell is equivalent to a Bloch wave at wave vector $\mathbf{s}$ with respect to the supercell.

The real-space supercell interpretation outlined above is instructive because upon inspection, it becomes apparent that there is no reason the matrix $\mathbf{M}$ must be diagonal. Any non-singular integer matrix $\mathbf{M}$ can be used to define the real-space supercell, and the coordinates of the generated *k*-points are then given by

$$\mathbf{k} = \begin{pmatrix} \mathbf{b}_1 & \mathbf{b}_2 & \mathbf{b}_3 \end{pmatrix} \left(\mathbf{M}^{-1}\right)^{\mathbf{T}} \begin{pmatrix} n_1 \\ n_2 \\ n_3 \end{pmatrix} + \mathbf{s} \tag{2.10}$$

where n_1, n_2, and n_3 are integers. We will refer to *k*-point grids described by equation (2.10) as generalized Monkhorst-Pack grids. In these grids, the total number of *k*-points in the Brillouin zone is equal to the number of primitive cells in the real-space supercell.

Examples of generalized Monkhorst-Pack grids on a two-dimensional rectangular lattice are shown in Figure 2.1. The green 2×2 supercell in real space corresponds to a 2×2 *k*-point grid in reciprocal space. This grid is illustrative of the traditional approach for constructing *k*-point grids, in which the matrix $\mathbf{M}$ is diagonal. Removing the constraint that the matrix $\mathbf{M}$ must be diagonal enables the construction of the red and blue supercells and corresponding generalized *k*-point grids. The red and blue grids contain 3 and 2 *k*-points per reciprocal space unit cell respectively, with *k*-points that are more evenly spaced than would be achieved by 3×1 or 2×1 grids.

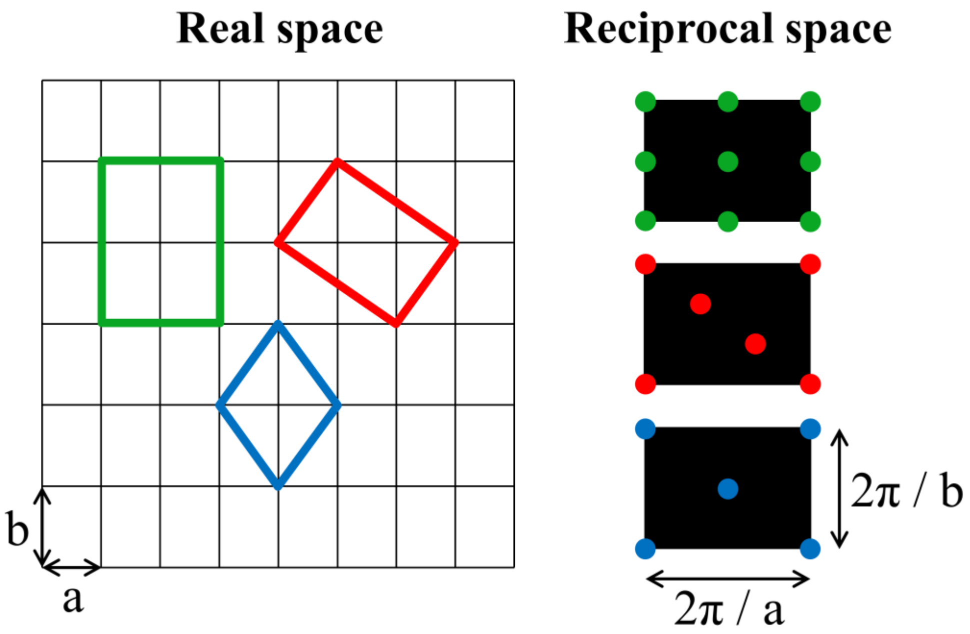

Figure 2.1. A comparison of (left) real-space supercells on a rectangle lattice and (right) the corresponding *k*-point grids in a unit cell of the reciprocal lattice. To aid visual comparison, all *k*-point grids are shifted so that one *k*-point falls on the corner of the reciprocal space unit cell.[63]. Figure adapted from ref. 45.

The benefit of using generalized grids was identified by Froyen[60], who suggested choosing the real-space supercell and shift vector in a way that minimizes the number of symmetrically irreducible *k*-points in the grid. Moreno and Soler demonstrated that generalized grids, as defined in equation (2.10), can always be expressed in terms of a diagonal matrix $\mathbf{M}$, provided the reciprocal lattice vectors $\mathbf{b}_1$, $\mathbf{b}_2$ and $\mathbf{b}_3$ are suitably chosen[61]. They expanded on Froyen's work by proposing the following approach for selecting the optimal *k*-point grid:

1) Select a minimum permissible distance between lattice points in the real-space superlattice. We will call this distance $r_{\min}$.
2) Of the possible superlattices in which all lattice points are separated by at least a distance of $r_{\min}$, find the one that corresponds to a *k*-point grid with the fewest symmetrically irreducible *k*-points.

There is intuitive appeal to the idea selecting *k*-point grids based on the minimum distance between points on the real-space superlattice. The density of the grid, and hence the speed and accuracy of the calculation, is determined by a single parameter, $r_{\min}$. The grid will also naturally be chosen so that the *k*-points are evenly distributed in reciprocal space. Specifically, this approach favors fcc-like real-space superlattices, resulting in bcc-like *k*-point grids.

Despite the apparent advantages of the *k*-point grid generation approach advocated by Moreno and Soler, it has seen little use in practice. It has been partially implemented in the SIESTA software package[62], but the partial implementation does not identify the grid with the fewest irreducible *k*-points. The relatively poor adoption of this approach, compared to the much more popular Monkhorst-Pack approach, is likely due to the fact that the Moreno-Soler approach mandates a search through all possible superlattices in which lattice points are separated by a distance of at least $r_{\min}$ to identify the one that results in the fewest number of irreducible *k*-points. This is significantly more complicated and computationally expensive than the relatively simple task of generating an $m_1 \times m_2 \times m_3$ Monkhorst-Pack grid.

2.2 Density Functional Theory

The following explanations is based on the book Sholl and Steckel[64]. DFT calculations aim to solve the time-independent, nonrelativistic Schrödinger equation, which is $\mathrm{H}\Psi = E\Psi$, where H is the Hamiltonian operator and Ψ represent the eigenstates. This many-body problem is expressed as:

$$\left[-\frac{\hbar}{2m}\sum_{i=1}\nabla_i+\sum_{i=1}^{N}V\left(r_i\right)+\sum_{i=1}^{N}\sum_{j<i}U\left(r_i,r_j\right)\right]\Psi = E\Psi \qquad (2.11)$$

$-\frac{\hbar}{2m}\sum_{i=1}\nabla_i$ represents the kinetic energy of each electron, $\sum_{i=1}^{N}V\left(r_i\right)$ represents the interaction energy between each electron and the collection of atomic nuclei, and $\sum_{i=1}^{N}\sum_{j<i}U\left(r_i,r_j\right)$ represents the interaction energy between different electrons. As Ψ , the wavefunction, is not directly observable, the quantity that we pay attention to is then the probability of the position of the electrons. This probability is represented by $\Psi^*\left(r_1,...,r_N\right)\Psi\left(r_1,...,r_N\right)$, where $r_1,...,r_N$ is a set of coordinates where electrons may be found and the asterisk indicating a complex conjugate. We can then define the density of electrons at a coordinate position r by:

$$n\left(r\right) = 2\sum_{i}\Psi_i^*\left(r\right)\Psi_i\left(r\right) \qquad (2.12)$$

with the factor of 2 representing the spin of the electrons.

By defining it as such, following the fundamental theorem by Hohenberg and Kohn[41]: “The ground state energy from Schrödinger’s equation is a unique functional of the electron density.” we can state the ground-state energy E in equation (3.12) as a functional of the electron density, i.e. $E\left[n\left(r\right)\right]$. This means that the property of the material can be defined as the ground-state electron density, which is a function described in three spatial variables. The functional itself is described by the second Hohenberg-Kohn theorem[41]: “The electron density that minimizes the energy of the overall functional is the true electron density corresponding to the full solution of the Schrödinger equation.”. This means that by minimizing the energy from the functional with the electron density, we would find the true electron density for the system. Writing this in terms of a group of single-electron wave functions, $\Psi_i\left(r\right)$, to define the electron density $n\left(r\right)$, the energy functional is then:

$$E\left[\left\{\Psi_i\right\}\right]=E_{known}\left[\left\{\Psi_i\right\}\right]+E_{XC}\left[\left\{\Psi_i\right\}\right] \tag{2.13}$$

where $E_{known}\left[\left\{\Psi_i\right\}\right]$ is a collection of analytical terms that we know and $E_{XC}\left[\left\{\Psi_i\right\}\right]$ is meant to group up other terms. $E_{known}\left[\left\{\Psi_i\right\}\right]$ can be defined as a combination of the electron kinetic energies, Coulomb interactions between electrons and nuclei, Coulomb interaction between electrons, and Coulomb interaction between nuclei:

$$\begin{aligned}E_{known}\left[\left\{\Psi_i\right\}\right]=&-\frac{\hbar}{m}\sum_i\int\Psi_i^*\nabla^2\Psi_i d^3r+\int V\left(r\right)n\left(r\right)d^3\\&+\frac{e^2}{2}\iint\frac{n\left(r\right)n\left(r'\right)}{|r-r'|}d^3rd^3r'+E_{ion}\end{aligned}\quad. \tag{2.14}$$

Kohn and Sham[42] showed that the correct electron density can be solved through a set of equations where each equation involves a single electron:

$$\left[-\frac{\hbar}{2m} \quad . \quad . \; . \left(r\right)+V_H\left(r\right)+V_{XC}\left(r\right)\right]\Psi_i\left(r\right)=\varepsilon_i\Psi_i \tag{2.15}$$

where $V\left(r\right)$ represents the interaction between an electron and the electron nuclei. $V_H\left(r\right)$ expresses the Hartree potential that describes the repulsion between an electron and the electron density:

$$V_H\left(r\right)=e^2\int\frac{n\left(r'\right)}{|r-r'|}d^3r'\,. \tag{2.16}$$

However, the electron density would include the atom in question itself. This means $V_H\left(r\right)$ would have an unphysical portion where an electron interacting with itself. The correction to this term is lumped into $V_{XC}\left(r\right)$ together with other correctional terms and is defined as:

$$V_{XC}(r)=\frac{\partial E_{XC}\left(r\right)}{\partial n\left(r\right)}\,. \tag{2.17}$$

The combination of this leads to a chicken-and-egg problem, in which to solve the Kohn-Sham equation one would need to define the Hartree potential, which requires the electron density, which requires the single electron wave functions, which in turn requires the solving the Kohn-Sham equation. This is solved through a self-consistent iterative algorithm, as described by Sholl[64]:

1. Define an initial electron density, $n(r)$.
2. Solve the Kohn-Sham equation using the initial electron density to find the single particle wave function, $\Psi_i(r)$.
3. Calculate the electron density using the wave function from step 2.
4. Compare the calculated electron density from step 3 with the initial electron density from step 1. If they are the same, then the ground-state electron density has been found, otherwise, the initial electron density needs to be update and the entire process re-done.

All DFT calculations in this thesis utilized the DFT as implemented by the Vienna Ab-initio Simulation Package (VASP)[65-69].

2.3 Database generation

As mentioned in our paper[63], for three-dimensional crystalline systems with time-reversal symmetry, the symmetry of possible *k*-point grids is given by one of 24 centrosymmetric symmorphic space groups[70]. For the 21 of these space groups that are neither triclinic nor monoclinic, the angles between lattice vectors are fixed, and only the lengths of the lattice vectors may change. To represent these space groups, we generated a set of 9094 sample structures with different lattice parameters, where the length of the longest conventional lattice vector could be up to 16 times as long as the length of the shortest vector. For each sample structure, we generated all possible real-space superlattices with up to 1728 (12×12×12) total primitive cells for orthorhombic, tetragonal, trigonal, and hexagonal space groups, and 5832 (18×18×18) total primitive cells for cubic space groups. Approximately 1% of the symmetrically distinct superlattices generated in this way had the same point group symmetry as the primitive lattice. When combined with the shift vectors described below (or no shift vector), these superlattices ensure that the set of *k*-points and all symmetrically equivalent points form a regular grid. They also make full use of symmetry to reduce the number of irreducible *k*-points. For these reasons, they were used to generate all *k*-point grids in the database.

For each symmetry-preserving superlattice, we calculated $r_{lattice}$, defined as the minimum spacing between points on the superlattice. For each sample structure, we identified the subset of superlattices that are on the Pareto frontier with respect to $r_{lattice}$ and the number of irreducible *k*-points in the corresponding *k*-point grid (Figure 2.2); these are the superlattices for which there is no other superlattice that has greater (or equal) $r_{lattice}$ and for which the corresponding *k*-point grid has fewer irreducible *k*-points. For any superlattice that is not on the frontier, it is always possible to find one on the frontier that is superior with respect to $r_{lattice}$ and the number of irreducible *k*-points. For this reason, only the superlattices on the Pareto frontiers were used to generate the *k*-point grid database. The resulting database contains 58,151 *k*-point grids.

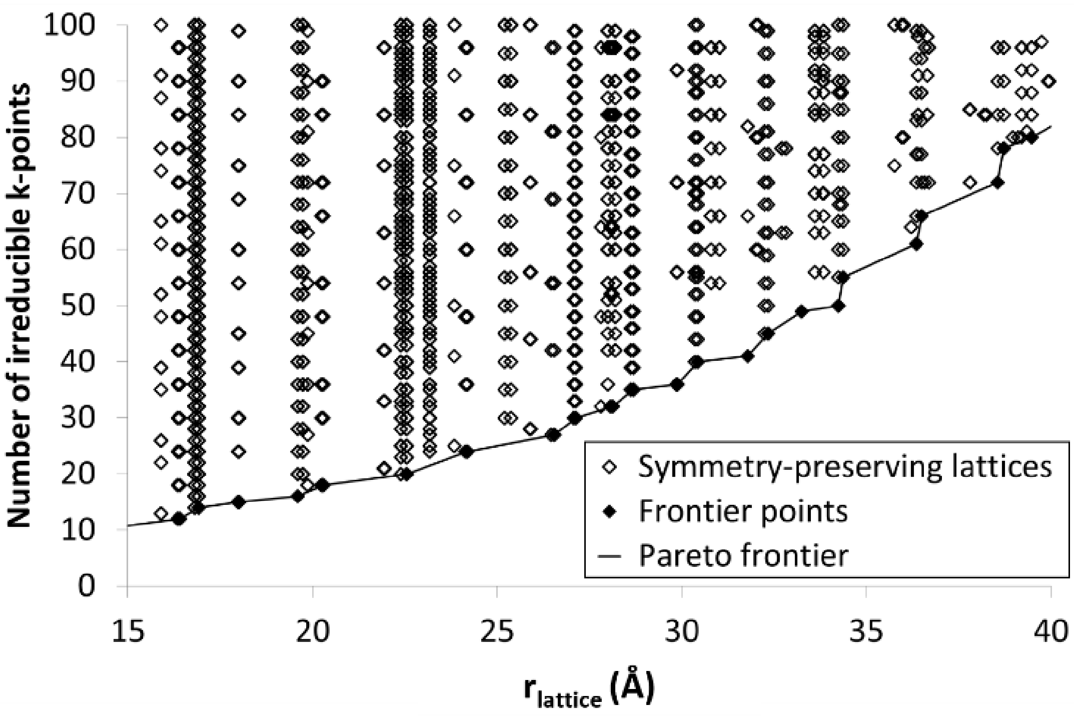

Figure 2.2. An example of a Pareto frontier used to identify the best *k*-point grids for a given structure. All symmetry-preserving lattices are indicated by diamonds, and the lattices on the frontier are indicated by black diamonds. For any lattice not on the frontier, it is always possible to find a better lattice, in terms of the number of distinct *k*-points and $r_{lattice}$, on the frontier.

2.3.1 Dynamic grid generation

For the triclinic and monoclinic space groups, we do not use a database due to the large number of lattices that would need to be included in the database and because the benefit of pre-calculating Pareto frontiers is relatively small for systems with low symmetry. Instead we dynamically identify the smallest superlattices for which $r_{\text{lattice}} > r_{\text{min}}$ and the point group symmetry matches that of the primitive lattice. Of these, we use the lattice that results in the fewest irreducible k-points.

2.3.2 *Large k-point grids*

To maintain fast performance for dynamic grid generation we currently limit our dynamic search to superlattices with no more than 216 total primitive cells. If no superlattice with 216 or fewer primitive cells is found, we identify the best superlattice for which $r_{\text{lattice}} > \frac{r_{\min}}{n}$, where the initial value of n is 2. If again no superlattice with 216 or fewer primitive cells is found, we iteratively increment n by 1 until we find a superlattice with no more than 216 primitive cells. We then return a *k*-point grid corresponding to a $n \times n \times n$ supercell of this superlattice. A similar method is used to generate lattices with more than 1728 *k*-points (for non-cubic space groups) and 5832 *k*-points (for cubic space-groups). For the results presented in this paper, convergence was always reached with $n = 1$.

2.4 Comparing different *k*-point generation methods

The following results and analysis section are taken from our paper that has been published previously in Physical Review Letters B[63].

2.4.1 *Benchmarking methodology*

We tested three different methods for generating *k*-point grids. The first, which we will refer to as the Generalized grid Database (GD), is the method described in the previous section. The second, which we will refer to as the Diagonal grid Database (DD), is the same as GD with the exception that the matrix $\mathbf{M}$ in equation (3.10) is constrained to be diagonal.

The two methods described above were compared to the automatic *k*-point generation scheme used in the Vienna Ab-initio Simulation Package (VASP)[65-69]. In this scheme, a Monkhorst-Pack grid is created where m_i, the number of grid points along the i^{th} reciprocal lattice vector $\mathbf{b_i}$, is determined by choosing a parameter *kspacing* and rounding $\frac{|\mathbf{b_i}|}{kspacing}$ up to the nearest integer. We will refer to this approach as a Simple Diagonal grid (SD). The SD method is representative of common approaches for generating Monkhorst-Pack grids.

In the DD and SD methods, the choice of the initial primitive cell is important, as the set of possible *k*-point grids is determined by the choice of lattice vectors for the primitive cell. We note that this is different from the GD method, for which identical *k*-point lattices are returned for any choice of the primitive lattice vectors. For all methods, we used Minkowski-reduced lattice vectors[71, 72] to represent all structures.

To generate shifted GD and DD grids (where the grid is shifted off the Γ point), the shift vector $\mathbf{s}$ was calculated as

$$\mathbf{s} = 0.5\mathbf{v}_1 + 0.5\mathbf{v}_2 + 0.5\mathbf{v}_3 \,. \qquad (2.18)$$

where $\mathbf{v}_1$, $\mathbf{v}_2$, and $\mathbf{v}_3$ are the lattice vectors of a conventional unit cell for the *k*-point grid. For structures with trigonal and hexagonal symmetry, the shift vector was constrained to be parallel to the three-fold rotational axis to avoid breaking symmetry. For the SD method, we used the Monkhorst-Pack method implemented in VASP, for which

$$\mathbf{s} = 0.5d_1\mathbf{b}_1 + 0.5d_2\mathbf{b}_2 + 0.5d_3\mathbf{b}_3 . \tag{2.19}$$

where $d_i = 1$ if m_i (the number of grid points in the i^{th} direction) is even, and $d_i = 0$ if m_i is odd. We explored the common practice of using unshifted (a.k.a. Γ-centered) grids instead of shifted grids for trigonal and hexagonal lattices, but we found that after correcting for fatal errors (as described below) this made the SD results worse.

For fcc materials, shifted grids generated using the DD method present a special case. When using a Minkowski-reduced primitive cell for an fcc lattice, it is impossible to generate a symmetry-preserving *k*-point grid that does not include the Γ point. This problem can be addressed by careful selection of the vectors used to define the primitive cell (in a way that is not Minkowski-reduced). As this is not commonly done in practice and would amount to manually creating a GD grid, we instead chose to include the Γ point for all "shifted" *k*-point grids generated using the DD method for fcc materials.

2.4.2 Benchmark calculations

To test for the effectiveness of our approach, we used density functional theory (DFT)[41, 42] as implemented in VASP to calculate the converged energies of 102 materials randomly selected from the Inorganic Crystal Structure Database (ICSD)[73] with fully occupied sites. Each structure was relaxed prior to the static calculations using a *k*-point grid with $r_{lattice}$ of at least 62 Å, which as seen in the main text is more than enough to achieve convergence. Structures that took more than 500 atomic steps to relax were discarded, as were structures for which VASP threw an error on unreasonable input geometry (i.e. "Sub-Space-Matrix is not hermitian" error). All relaxations were run spin-polarized. For materials that relaxed to a state with no net spin, the static benchmark calculations were run with no spin polarization. For materials that relaxed to a spin-polarized structure, spin polarization was used in all static benchmark calculations. To reduce the amount of noise due to structures relaxing to different spin states, in all benchmark calculations the net spin of each material was fixed to a constant value calculated by rounding the net spin of the final relaxed state to the nearest integer.

For the static benchmarking calculations, energies were converged to a difference of less than 10^{-5} eV per unit cell. Across all grid generation methods, some calculations produced anomalous energies at even fairly dense *k*-point grids, introducing substantial noise to the results. All of these calculations had both of the following warnings in their output files:

```
WARNING: DENTET: can't reach specified precision

BRMIX: very serious problems
 the old and the new charge density differ
```

The problem was fixed by re-running the calculations using Gaussian smearing (with a width of 0.05 eV) instead of the tetrahedron method. This fix was used on all 496 calculations that had both of the above warnings.

Even after the fix described above, there were two structures that failed to reach electronic self-consistency after 150 electronic steps at grid densities that could have affected the convergence results. This behavior was observed for all grid generation methods. These materials were discarded, and the remaining 102 structures, shown in the Table 2.1 below, were used for benchmarking.

ICSD ID	Arithmetic Crystal Class	Composition	Is Metal	Number of Atoms in Unit Cell	Unit Cell Volume (Å^3)
56545	19	AgCl	FALSE	4	75.72
159858	41	Ag_3IS	FALSE	5	118.29
8117	18	$AlCl_4Na$	FALSE	24	615.01
92522	50	$AlLaO_3$	FALSE	10	108.65
70109	49	AlO_4P	FALSE	18	223.19
14270	8	Al_4CaO_7	FALSE	24	294.81
36478	18	$AsCuPbS_3$	FALSE	24	553.31
16145	18	As_4S_3	FALSE	28	781.53
98792	7	As_8S_9	FALSE	34	893.45
412235	7	$Au_3F_{18}Sb_2$	FALSE	46	594.25
613405	58	BCo_4Y	TRUE	12	145.31
613529	36	B_2CrNb_2	TRUE	10	114.06
44431	58	B_2LaRh_3	TRUE	6	82.44
615671	21	B_4V_3	TRUE	7	59.26
172338	8	$BaC_2F_6O_6S_2$	FALSE	34	479.50
108831	18	$BaCuO_5Y_2$	FALSE	36	488.57

ICSD ID	**Arithmetic Crystal Class**	**Composition**	**Is Metal**	**Number of Atoms in Unit Cell**	**Unit Cell Volume (Å^3)**
25311	37	$BaMg_2Si_2$	TRUE	5	118.10
74006	8	$BaMn_2O_{14}Si_4Sr_2$	FALSE	23	289.90
155512	27	BaO_4W	FALSE	12	190.90
108097	71	BaTe	FALSE	2	72.82
162894	49	$Ba_3Fe_3NbO4Si_2$	FALSE	23	327.92
75963	19	$Ba_5ClO_9Ru_2$	FALSE	34	563.21
180893	37	$BiNi_2O_{10}Sr_5$	TRUE	18	246.33
155011	36	BrFPb	FALSE	6	132.58
29114	36	$Br_2CO_3Pb_2$	FALSE	32	626.01
618234	58	CLu_5Si_3	TRUE	18	362.99
420223	8	CS_3Tl_2	FALSE	12	301.71
85953	71	C_7V_8	TRUE	60	572.70
170824	8	$CaCuGe_2O_6$	TRUE	20	239.51
159035	19	$CaIrO_3$	TRUE	10	112.23
168903	71	$CaMnO_3$	TRUE	5	51.72
182052	49	Ca_2O_4Si	FALSE	14	179.38
96484	50	Ca_3FeO_6Rh	FALSE	22	257.54
183509	72	CdS	FALSE	2	50.96
81658	18	$Cd_3K_2Te_4$	FALSE	36	1253.50

ICSD ID	Arithmetic Crystal Class	Composition	Is Metal	Number of Atoms in Unit Cell	Unit Cell Volume (Å^3)
82547	18	CeGeRh	TRUE	12	234.21
622339	58	$CeZn_5$	TRUE	6	104.05
420548	18	ClO_3PbV	FALSE	24	374.94
90123	37	$Cl_2Co_2O_5Sr_3$	TRUE	12	178.03
65731	72	Cl_6Cs_2LiY	FALSE	10	283.07
64613	72	Cl_6Cs_2Re	FALSE	9	268.20
27180	7	$Cl_6H_{22}O_{10}Sn$	FALSE	78	820.07
26692	72	Cl_6Rb_2Se	FALSE	9	247.82
624863	18	CoSSb	FALSE	24	403.92
249347	18	Cs_2S_4W	FALSE	28	958.93
261952	7	$Cs_4Ge_8O_{20}U$	TRUE	66	1112.96
28737	37	$CuGaSe_2$	FALSE	8	177.97
657666	37	$CuInSe_2$	FALSE	8	201.40
75531	72	$CuIr_2S_4$	TRUE	14	243.76
65677	21	$CuLiO_4V$	FALSE	14	141.18
86752	37	$CuNd_2O_4$	TRUE	7	90.95
247127	41	CuO_3Si	TRUE	30	462.08
280597	72	Cu_6O_8Pb	TRUE	15	156.56
631453	8	Eu_2O_3	TRUE	15	220.41

ICSD ID	Arithmetic Crystal Class	Composition	Is Metal	Number of Atoms in Unit Cell	Unit Cell Volume (Å^3)
37448	41	F_6NiPt	FALSE	8	91.25
20029	18	F_8K_2Re	FALSE	44	582.58
169262	58	FeSe	TRUE	4	61.53
37124	18	Fe_2MoP_{12}	FALSE	60	868.85
15840	50	Fe_2O_3	TRUE	10	86.23
420235	21	$Fe_2O_5Sr_3$	TRUE	10	138.39
1118	2	$Fe_3Na_7O_8$	FALSE	36	474.65
106712	72	Ga_2LiPd	TRUE	4	57.77
100052	50	Ga_2Li_3	TRUE	5	76.39
167567	36	$Ga_4Mn_3Ni_9$	TRUE	16	190.40
39788	18	$GeNaO_5Sb$	FALSE	64	878.91
60943	18	H_2O_4Se	FALSE	28	298.03
169603	37	H_2Ti	TRUE	3	21.22
240915	18	H_4I_3NPb	FALSE	36	926.89
418251	7	$H_4Li_2O_6P$	FALSE	52	444.94
2226	7	H_5NaO_4S	FALSE	88	866.11
170776	62	$H_7NO_{13}P_3Ti_2$	TRUE	104	957.40
174108	18	HfO_3Pb	FALSE	40	555.23
640117	58	InNi	TRUE	6	95.24

ICSD ID	Arithmetic Crystal Class	Composition	Is Metal	Number of Atoms in Unit Cell	Unit Cell Volume (Å^3)
174222	7	IrP_2	FALSE	12	185.17
104572	72	Ir_2Th	TRUE	6	114.65
641029	21	$Ir_3Si_5Y_2$	TRUE	20	332.47
602269	36	KMnSb	TRUE	6	175.29
82227	18	$LaMnO_3$	TRUE	20	236.69
641459	41	$LaMo_6Se_8$	TRUE	15	314.31
641499	19	LaNi	TRUE	4	90.31
420918	8	$La_5NO_2S_4$	FALSE	24	527.60
642364	49	$LiSe_2Zr$	TRUE	4	79.09
83791	18	Mg_2O_4Si	FALSE	28	275.45
159441	58	MoN	TRUE	2	20.23
167863	72	NOs	TRUE	2	20.58
35198	27	NaO_3P	FALSE	40	492.77
92128	50	NiO	TRUE	2	18.00
657414	50	Ni_3S_2	TRUE	5	66.76
50942	18	$O_{12}Sc_2W_3$	FALSE	68	1156.49
41474	49	O_2Si	FALSE	9	93.89
169629	36	O_2Ti	FALSE	6	62.90
79914	18	O_2Zr	FALSE	12	120.33

ICSD ID	Arithmetic Crystal Class	Composition	Is Metal	Number of Atoms in Unit Cell	Unit Cell Volume (Å^3)
33803	37	$O_7Ru_2Sr_3$	TRUE	12	156.13
36630	19	$P_5Pd_5Sr_4$	TRUE	28	566.04
105719	58	Pd_5Th_3	TRUE	8	172.54
167651	36	Pd_5Ti_3	TRUE	8	124.90
162013	37	$PrRh_2Si_2$	TRUE	5	84.51
650389	71	$Rh_4Sn_{13}Sr_3$	TRUE	40	967.62
38354	71	S_3U_4	TRUE	7	155.61
651499	71	Sb	TRUE	1	29.84
167903	73	Ta	TRUE	1	18.05
653446	72	W_2Zr	TRUE	6	109.68

Table 2.1. List of all 102 structures taken randomly from the ICSD and used to benchmark the server along with their arithmetic crystal class, composition, number of atoms and volume[63]. Table adapted from the supplemental information of ref. 45.

To determine the number of *k*-points required to calculate a converged energy value, we generated *k*-point grids for 33 different values of $r_{\min}$ for each material using each of the three different methods. These grids were generated by starting from $r_{\min} = 100$ Å and incrementally reducing $r_{\min}$ by a factor of $2^{1/6}$ until we reached $r_{\min} = 2.48$ Å. For the SD method, we used $kspacing = \frac{2\pi}{r_{\min}}$. The lower limit of

$r_{\min} = 2.48$ Å was chosen to ensure that for all materials, the least-dense DD and GD grids contained exactly one irreducible *k*-point. For four materials, a lower value of $r_{\min}$ was required to generate a SD grid with exactly one irreducible *k*-point, but generating grids using $r_{\min} < 2.48$ Å would not have changed the convergence results for any of those materials.

We used the projector augmented wave (PAW)[74] potentials provided with VASP. For all elements, we used the GW version of the potentials. All VASP calculations were run with PREC=Accurate, avoiding wrap-around errors in the Fourier transform.

For the electronic self-consistency loop, we chose ALGO = FAST. This setting uses a blocked Davidson iteration scheme for the first five electronic minimization steps, followed by a residual minimization scheme, direct minimization in the iterative subspace (RMM-DIIS). The RMM-DIIS algorithm caused an error in 1138 out of our total of 20196 calculations. For these 1138, we switched to a pure blocked Davidson iteration scheme (i.e. ALGO = NORMAL).

All calculations were done using the tetrahedron method with Blöchl corrections[75] except for when there were less than 4 irreducible points; in this case Gaussian smearing with a width of 0.05 eV was used. For each grid, we calculated the error, Δ_{grid}, as the absolute difference between the calculated energy per atom and that calculated using the densest grid. The calculation was considered to be converged at the least-dense grid for which Δ_{grid} for all grids with greater or equal density was less than the maximum acceptable error. For all grid-generation methods, anomalously high values of Δ_{grid} were observed for some calculations that had both BRMIX and DENTET warnings in VASP. All 496 calculations that had both BRMIX and DENTET warnings were re-run using Gaussian smearing, which removed the anomalous results.

For nearly 40% of the shifted grids generated using the SD method, VASP threw fatal errors. In such cases, as if often done in practice, the shifted grid was replaced with a Γ-centered grid. For four calculations, using SD Γ-centered grids with $r_{\min} = 100$ Å (the densest grids), VASP threw fatal errors or stalled. In these cases, energy was replaced by the average of the energies of the densest grids generated using other methods. Because there was little variation in the energies per atom for the densest grids, we do not believe this substitution significantly affected our results. For calculations using the DD and GD *k*-point grids, VASP did not throw fatal errors for any of the 13,332 calculations.

2.4.3 Benchmarking results

For the three different methods, the average number of irreducible *k*-points required to reach different levels of convergence for the calculated energy is shown in Figure 2.3. For convergence of the energy within 1 meV / atom, the SD method required on average 2.25 times as many irreducible *k*-points as the GD method for Γ-centered grids and 2.69 times as many for shifted grids. Most of the gain appears to come from the uses of high-symmetry grids and the Pareto frontier, as the DD method also shows significant gains over the SD method, despite the fact that both methods result in "diagonal" grids aligned with the reciprocal lattice vectors. The relative advantage of the DD and GD methods over the SD method increases as the convergence criterion is tightened. This is primarily because the benefit of using highly symmetric grids, in terms of the reduction in the total number of irreducible *k*-points, is greater for grids that have a large number of total *k*-points.

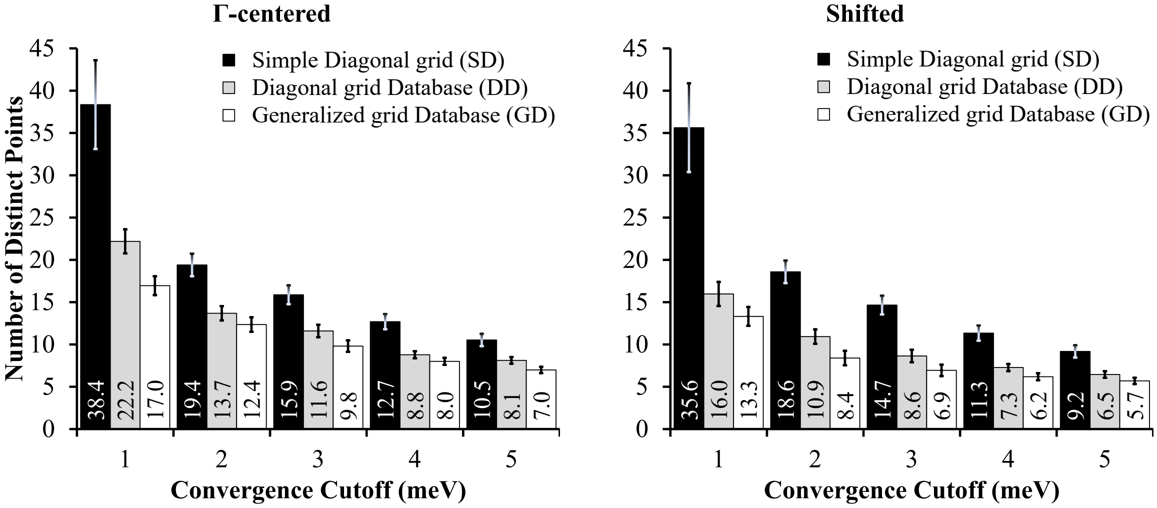

Figure 2.3. The average number of distinct k-points required to reach convergence within different levels of accuracy for different grid-generation methods. Error bars represent the standard error of the mean.[63]. Figure adapted from ref. 45.

The reduction in the total number of irreducible *k*-points is reflected in a reduction in average computational cost. To estimate the computational cost, we assumed that the calculation time scales linearly with the number of *k*-points; analysis of the benchmark calculations supported this assumption. To minimize the noise in benchmark times due to e.g. running on different nodes at different times, for each material a single value for the average CPU time per *k*-point was used for all methods. This value was taken from the converged SD calculation using a Γ-centered grid. The benchmark time was then calculated as the number of irreducible *k*-points multiplied by the CPU time per *k*-point for the material, effectively weighting the number of irreducible *k*-points by a material-specific computational cost per *k*-point.

The average runtimes, relative to the runtimes for the GD method, are shown in Figure 2.4. The trends are similar to those for the average number of irreducible *k*-points. For Γ-centered grids, the GD method is about 50-100% faster than the SD method. For shifted grids, the difference is much greater. This is likely due to the facts that the SD shifted grids include a mix of calculations using shifted and Γ-centered grids, and the SD method determines the shifts differently than the GD or DD methods. The speed-up when going from DD grids to GD grids is roughly the same for both Γ-centered and shifted grids.

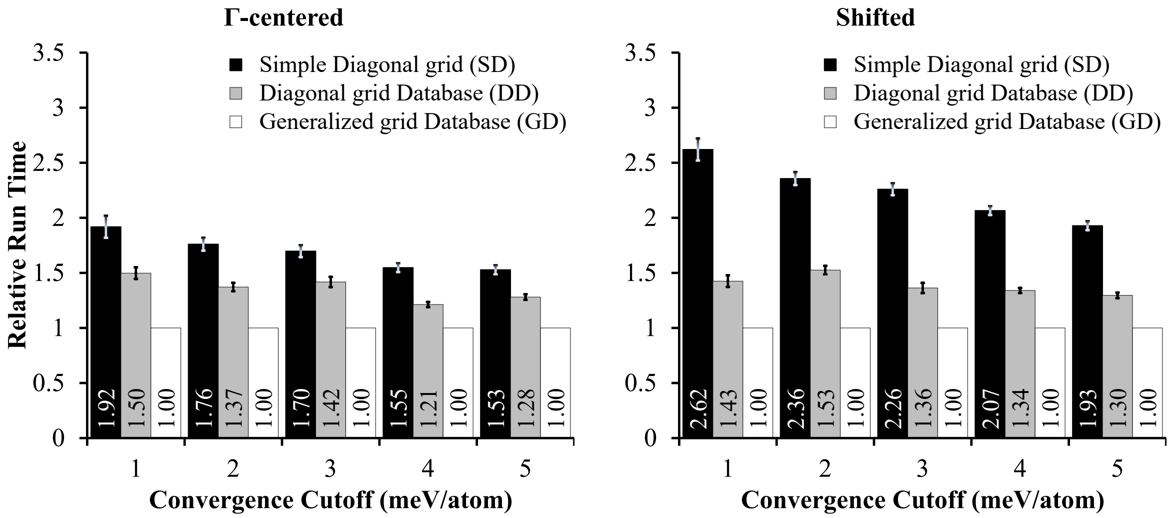

Figure 2.4. The average relative run times required to reach convergence within different levels of accuracy for different grid-generation methods. The GD method was used as the reference value for both Γ-centered and shifted runs. Run times were calculated in CPU-hours. Error bars represent the standard error of the mean.[63]. Figure adapted from ref. 45.

For high-throughput calculations, the average total CPU time per material (Figure 2.5) is the metric that determines the throughput. Shifted grids consistently resulted in lower CPU times, even for the SD method. To reach 1 meV / atom convergence, the GD shifted grids resulted in 2.78 times the throughput as SD Γ-centered grids, and 1.95 times the throughput as SD shifted grids. The average total performance gains shown in Figure 3.5 are generally not as large as the average relative performance gains shown in Figure 3.4. This is primarily because the average total performance gains are effectively weighted by the CPU time for each material, and for some materials with large CPU times, such as those with large unit cells for which only one irreducible *k*-point is needed, there is relatively little difference among the three different methods.

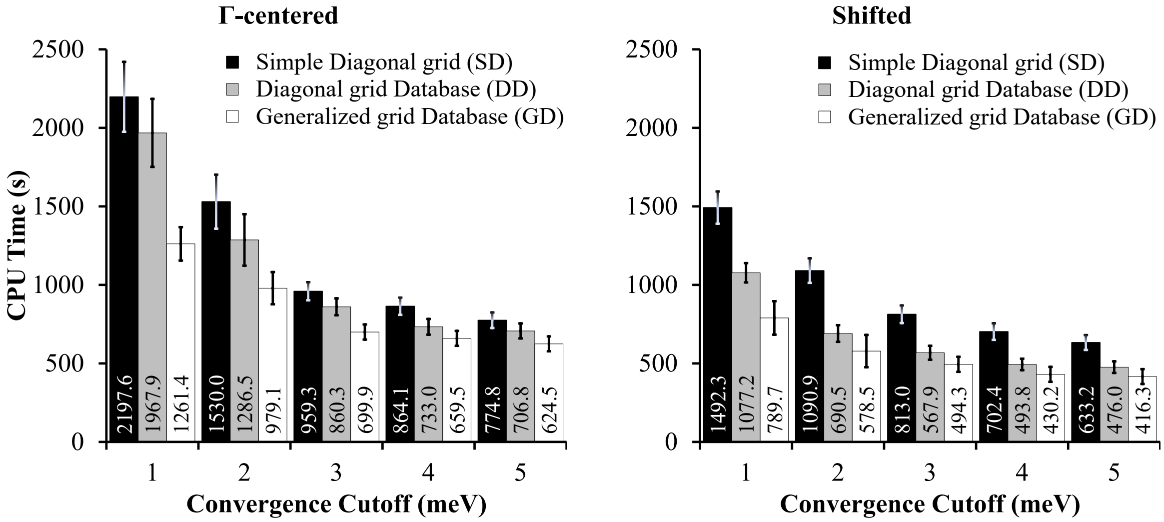

Figure 2.5. The average computational time required to reach convergence within different levels of accuracy for different grid-generation methods. Error bars represent the standard error of the mean.[63]. Figure adapted from ref. 45.

2.5 Determining minimum periodic distance, $r_{\min}$

In the Moreno-Soler approach, the speed and accuracy of the calculation are determined by the parameter $r_{\min}$, the minimum acceptable distance between points on the real-space superlattice. Ideally, for a given material system, the user would test different values of $r_{\min}$ to identify the smallest value at which the calculation is sufficiently accurate. However in practice, it is helpful to use a heuristic that allows for rapid estimation of a reasonable value for $r_{\min}$. This is especially true for high-throughput calculations, in which the selection of the *k*-point grid is entirely automated and separately testing for *k*-point convergence for every material could be prohibitively expensive. Here we discuss several approaches for estimating the appropriate value for $r_{\min}$.

2.5.1 General trends

We start by examining how the error in our set of 102 benchmark materials varies as a function of $r_{\min}$. We consider two measures of the error: the average absolute error across all 102 materials, and the maximum absolute error across all 102 materials. We divide our analysis into two classes of materials: metals, defined as those materials for which there is no indirect band gap for a DFT calculation using the densest Γ-centered GD grid (i.e. $r_{\min} = 100$ Å), and non-metals, defined as all other materials. There are 50 metals and 52 non-metals in the benchmark set. To calculate the errors used in this analysis, we use shifted GD grids, as we expect they will be the most widely used due to their superior efficiency.

The average absolute error, maximum absolute error, and average CPU time as a function of $r_{\min}$ are presented in Figure 2.6. For non-metals, the maximum error is 20.5 meV / atom at $r_{\min} = 15.7$ Å and it drops sharply to 6.8 meV / atom at $r_{\min} = 17.7$ Å. At $r_{\min} = 17.7$ Å the average absolute error falls to 0.4 meV / atom. This suggests that absolute errors of less than about 10 meV / atom can be achieved across a large percent of non-metals with $r_{\min} \approx 18$ Å. At a slightly higher value of $r_{\min} = 19.8$ Å, the maximum absolute error falls to 2.4 meV / atom and the average absolute error falls to 0.3 meV / atom. The absolute error falls below 1 meV / atom for all non-metals at $r_{\min} = 31.5$ Å. For metals, larger values of $r_{\min}$ are required to reach similar levels of accuracy, as expected. The maximum absolute error does not fall below 10 meV / atom until $r_{\min} = 28.1$ Å. At $r_{\min} = 35.4$ Å, the maximum absolute error falls to 1.5 meV / atom, and at $r_{\min} = 50.0$ Å the maximum absolute error is 0.6 meV / atom.

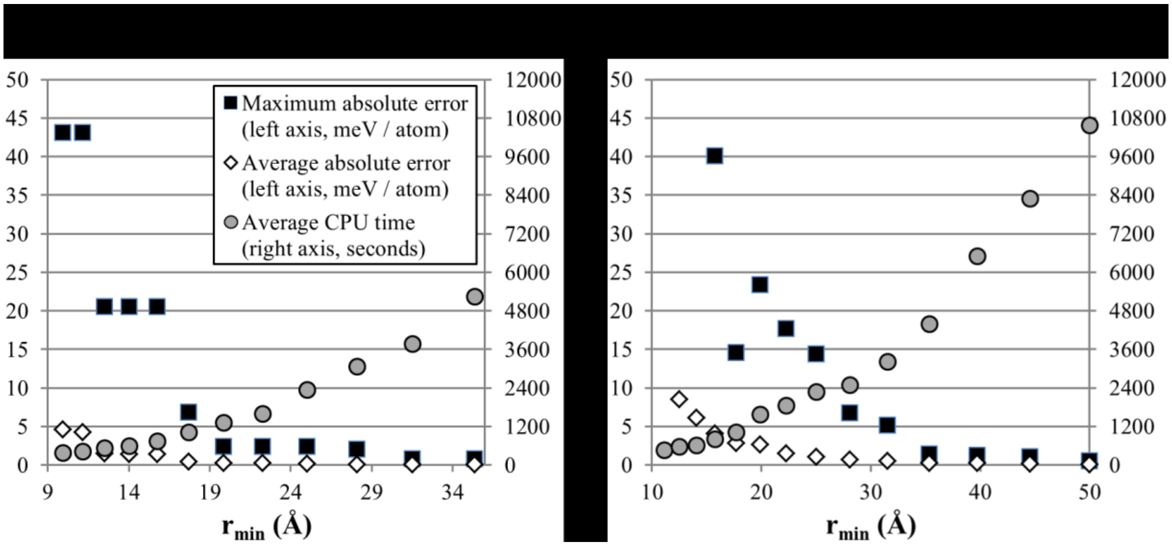
[redacted]

Figure 2.6. The maximum absolute error (black squares, left axis), average absolute error (white diamonds, left axis), and average CPU time (grey circles, right axis) for metals and non-metals as a function of $r_{\min}$ [63]. Figure adapted from ref. 45.

We have also calculated the fraction of the calculations that converge within a given level of accuracy as a function of $r_{\min}$ (Figure 2.7). For non-metals, 100% of the calculations had converged within 3 meV / atom, and 92.3% had converged within 1 meV / atom, at $r_{\min} = 19.8$ Å. The results are only slightly worse at $r_{\min} = 17.7$ Å, where 98.1% have converged within 3 meV / atom and 100% have converged within 10 meV / atom. Under the assumption that computational cost scales linearly with the number of irreducible *k*-points, calculations at $r_{\min} = 19.8$ Å can be expected to take approximately 40% longer than calculations at $r_{\min} = 17.7$ Å, so the computational cost savings from reducing $r_{\min}$ might be enough to justify the small loss of accuracy.

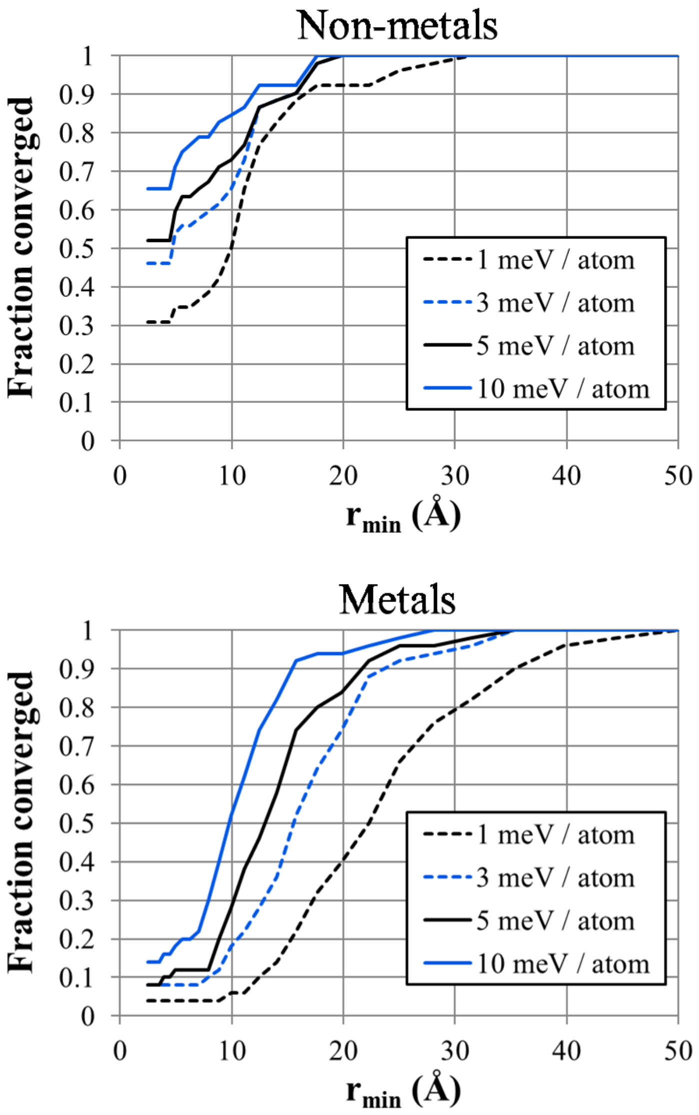

Figure 2.7. The fraction of calculations for non-metals and metals that have reached convergence within different levels of accuracy as a function of $r_{\min}$ [63]. Figure adapted from ref. 45.

For metals, the first point at which 100% of the calculations converged within 1 meV / atom is at $r_{\min} = 50\ \text{Å}$. At $r_{\min} = 35.4\ \text{Å}$, all metals had converged within 3 meV / atom, and all had converged within 10 meV / atom at $r_{\min} = 28.1\ \text{Å}$. At this value, the maximum absolute error for metals in our data set is 6.8 meV / atom, and the average absolute error is 0.7 meV / atom. At $r_{\min} = 28.1\ \text{Å}$, all non-metals are converged within 3 meV / atom. Thus $28.1\ \text{Å}$ might be a reasonable default value of $r_{\min}$ for calculations in which the existence of a band gap in the material is unknown and reasonably accurate energies are desired. However we note that calculations at $r_{\min} = 28.1\ \text{Å}$ can be expected to cost, on average, about 4 times as much as calculations at $r_{\min} = 17.7\ \text{Å}$, demonstrating that prior knowledge of the existence of a band gap can significantly reduce the required computational time.

The above results were generated for our sample of 102 random materials, and the subsets of metals and non-metals only contain about 50 materials each. To reach any given level of accuracy, there are almost certainly materials that require larger values of $r_{\min}$ than any material in our data set. This is important to keep in mind for some applications, such as phase diagram calculations, in which a single material with a large error in its calculated energy can dramatically affect the outcome. If close to 100% convergence within a given level of accuracy is required, we advise using values of $r_{\min}$ that are larger than those indicated in Figure 2.7.

2.5.2 As a function of the band gap for non-metals

For reasons discussed in section II.A, in the limit of large $r_{lattice}$, the error due to *k*-point sampling will decay as $e^{-\gamma r_{lattice}}$ for materials with a band gap. The rate of decay, γ, will be determined by the decay rate of the Hamiltonian matrix elements between Wannier functions, which can be expected to be the same as the rate of decay for the density matrix[76,

[77]. In the weak-binding limit, the exponential decay rate of the density matrix is expected to be proportional to E_{gap}, the direct band gap of the material[77, 78]. Thus it can be expected that in the weak-binding limit, the value of $r_{\min}$ required to reach a given level of convergence will vary roughly inversely with the direct band gap. In the tight-binding limit (materials with a large band gap), the relationship between γ and E_{gap} has not been well established[77].

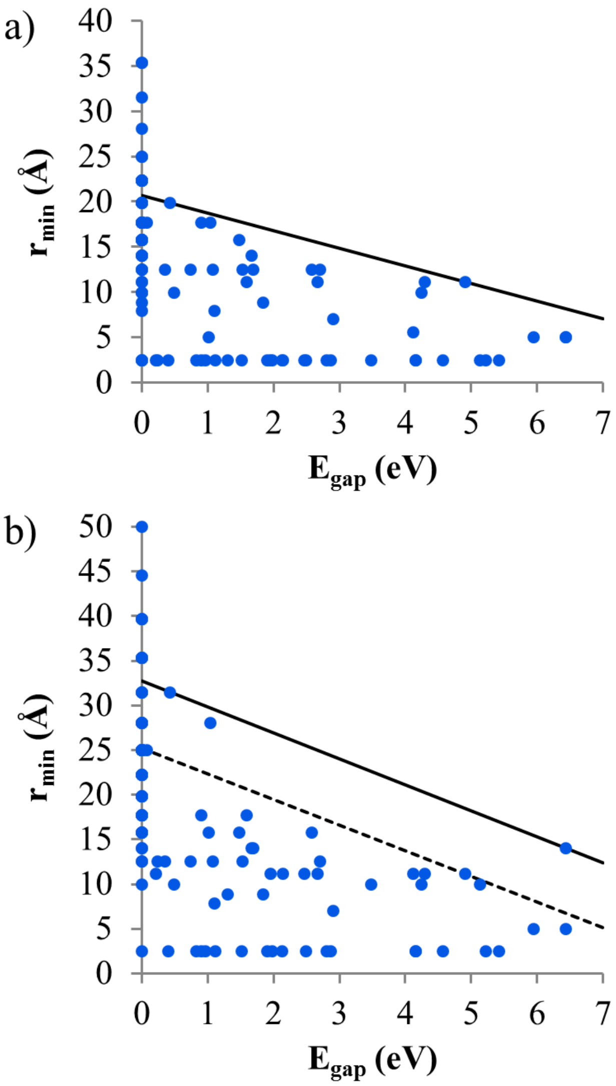

Figure 2.8. The relationship between the direct band gap (E_{gap}) and the value of $r_{\min}$ at which convergence was reached within a) 3 meV / atom b) 1 meV / atom. The solid diagonal line in a) is a plot of equation (3.12). The solid diagonal line in b) is a plot of equation (3.13), and the dashed diagonal line in b) is a plot of equation (3.14)[63]. . Figure adapted from ref. 45.

For the 102 structures in our data set, we plot the relationship between E_{gap} (the direct band gap) and the value of $r_{\min}$ required to reach convergence within 3 meV / atom in Figure 3.8a. For these plots, E_{gap} was calculated using DFT with a Γ-centered GD *k*-

point grid at the maximum density ($r_{\min} = 100$ Å). The value of $r_{\min}$ at which convergence was reached was calculated using shifted GD grids. As expected, average values for $r_{\min}$ decrease as E_{gap} increases. The upper edge of the scatterplot in Figure 3.8 is roughly linear, and we find that all non-metals in our benchmark set would be converged within 3 meV / atom if $r_{\min}$ were at or above the value calculated using the following equation:

$$r_{\min} = 20.69 - 1.95\left(E_{gap}\right) \tag{2.20}$$

where $r_{\min}$ is in Angstroms and E_{gap} is expressed in eV. Similar analysis for convergence levels of 4 meV / atom and 5 meV / atom yield the same equation.

To reach a convergence level of 1 meV / atom for all non-metals in our data set (Figure 3.8b), the following equation could be used to set $r_{\min}$:

$$r_{\min} = 32.76 - 2.91\left(E_{gap}\right). \tag{2.21}$$

If equation (2.20) were used to set $r_{\min}$ instead of equation (2.21), 86.5% of the non-metals would still be converged within 1 meV / atom. As a compromise between the two approaches, the following equation would converge all non-metals within 3 meV / atom and 94.2% within 1 meV / atom:

$$r_{\min} = 25.22 - 2.87\left(E_{gap}\right). \tag{2.22}$$

The lines represented by equations (2.20), (2.21), and (2.22) are all plotted in Figure 3.8.

In practice, good estimates for E_{gap} are often not available before a calculation has been run, but there is often a sense of whether a material is a semiconductor or a large band-gap insulator. For all materials in our data set with E_{gap} of more than 0 eV and less than 2 eV, we note that $r_{\min} = 20$ Å would be sufficient to reach convergence within 3 meV / atom. For materials in our data set with E_{gap} greater than 2 eV, $r_{\min} = 12.5$ Å would be sufficient.

2.5.3 Relationship with other methods

In some cases, particularly for high-throughput calculations, an automated method already exists for determining *k*-point grids. It is helpful to consider how such methods relate to the method described in this paper. For example, an alternative to using $r_{\min}$ to determine the grid density is to require that the grid contains at least N_{kpt} *k*-points in the Brillouin zone, where N_{kpt} is calculated separately for each material. It is straightforward to find a value for $r_{\min}$ that guarantees that this condition is met. For a given value of $r_{\min}$, the number of total *k*-points will be minimized by generating an fcc real-space superlattice. Thus the following value of $r_{\min}$ will ensure that there are at least N_{kpt} total *k*-points in the Brillouin zone:

$$r_{\min} = \left(N_{kpt} \times V_{prim} \times 2^{1/2}\right)^{1/3}. \tag{2.23}$$

With $r_{\min}$ given by equation (2.23), in some cases the search along the Pareto frontier might discover a grid with significantly more than N_{kpt} total *k*-points but relatively few irreducible *k*-points. Such a grid can be expected to result in particularly low *k*-point approximation error at a low computational cost.

A second approach to choosing values for $r_{\min}$ in a way that is consistent with other methods is to match the percentage of calculations that converge within a given level of accuracy. For example, consider a hypothetical method for generating *k*-point grids which results in energy convergence within 5 meV / atom 90% of the time. We could define an equivalent value of $r_{\min}$ as that which would result in the same convergence rate.

We illustrate the second approach by first considering the relationship between $r_{lattice}$ and the number of *k*-points per reciprocal atom ($kAtom$). The Materials Project[79], Aflowlib[80], and Open Quantum Materials Database[81] all use $kAtom$ to set the density of *k*-point grids. For each of the 102 materials in our database, we identified the shifted GD *k*-point grids at which the calculation had converged within 1 meV / atom. For each of these grids we calculated both $kAtom$ and $r_{lattice}$ (based on the corresponding real-space superlattice). We then generated two sorted lists of *k*-point grids: the first sorted according to $kAtom$, and the second sorted according to $r_{lattice}$. Each was sorted from smallest to largest.

Let k_n represent the value of $kAtom$ for the n^{th} item on the first list. If grids with $kAtom = k_n$ were generated for all 102 materials, calculations using these grids for the first $n-1$ materials on the first list would be expected to be converged within 1 meV / atom, and calculations using these grids for the remaining $102-n$ materials would not. Similarly, let r_n represent the value of $r_{lattice}$ for the n^{th} item on the second list. If grids with $r_{lattice} = r_n$ were generated for all 102 materials, calculations using these grids for the first $n-1$ materials on the second list would be expected to be converged, and calculations using these grids for the remaining $102-n$ materials would not. Thus using a lower bound of $kAtom_{\min} = k_n$ k-points per reciprocal atom can be expected to yield about the same percentage of converged calculations as setting $r_{\min} = r_n$.

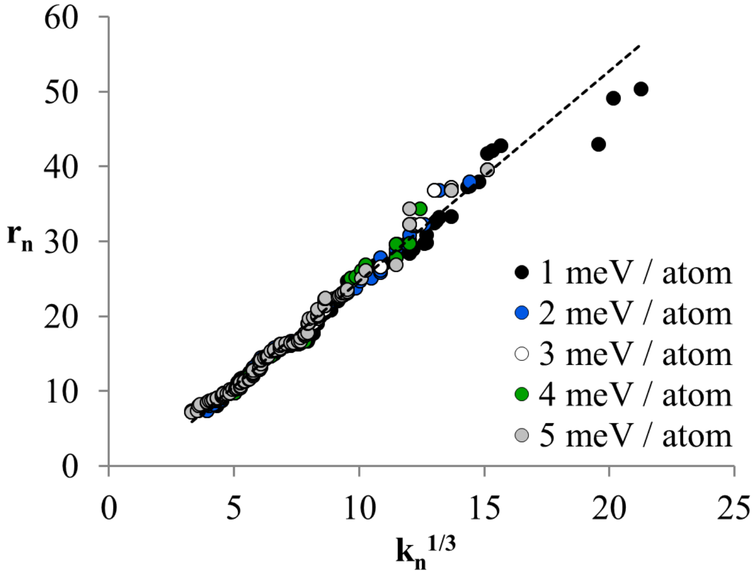

Figure 2.9. A plot of $k_n^{1/3}$ vs. r_n for sorted lists generated at five different levels of convergence. For the n^{th} point on each list, there are $n-1$ materials that converged with a lower (or equal) value of r_n and $n-1$ materials that converged with a lower (or equal) value of k_n. The diagonal dashed line illustrates the best linear fit to all 510 points, given by equation (3.17)[63]. Figure adapted from ref. 45.

In Figure 2.9, we plot r_n vs $k_n^{1/3}$ for five different levels of convergence: 1, 2, 3, 4, and 5 meV / atom. The relationship is nearly linear and along the same line for all five levels of convergence. Linear regression yields the following estimate for r_n as a function of $k_n^{1/3}$, with $R^2 = 0.988$:

$$r_n \approx 2.8074\left(k_n^{1/3}\right) - 3.4008 \tag{2.24}$$

Equation (2.24) allows us to establish a relationship between $kAtom_{\min}$, the minimum allowed number of *k*-points per reciprocal atom, and $r_{\min}$, the minimum allowed value of $r_{lattice}$ (Figure 2.10a). For example, a minimum of 1000 *k*-points per reciprocal atom corresponds to $r_{\min} = 24.7\ \text{Å}$, and a minimum of 7000 *k*-points per reciprocal atom corresponds to $r_{\min} = 50.3\ \text{Å}$.

We have done similar analysis for two other metrics for *k*-point grid density: the number of *k*-points per reciprocal cubic Angstrom ($kVol$) and the length of the longest vector in the Minkowski-reduced representation of the *k*-point lattice in reciprocal space ($kDist$). We note that $kDist$ is similar to the $kspacing$ value used by VASP. The relationship between r_{n} and $kVol_{\text{n}}$ ($R^2 = 0.993$) is

$$r_{\text{n}} \approx 1.0688\left(kVol_{\text{n}}^{1/3}\right) - 2.5877\,, \tag{2.25}$$

and the relationship between r_{n} and $kDist_{\text{n}}$ ($R^2 = 0.994$) is

$$r_n \approx 1.0265\left(\frac{2\pi}{kDist_n}\right) + 1.0183\,. \tag{2.26}$$

Based on equations (2.25) and (2.26), the estimated equivalent values of $r_{\min}$ for different values of $kVol_{\min}$ and $kDist_{\max}$ are shown in Figure 2.10b and Figure 2.10c.

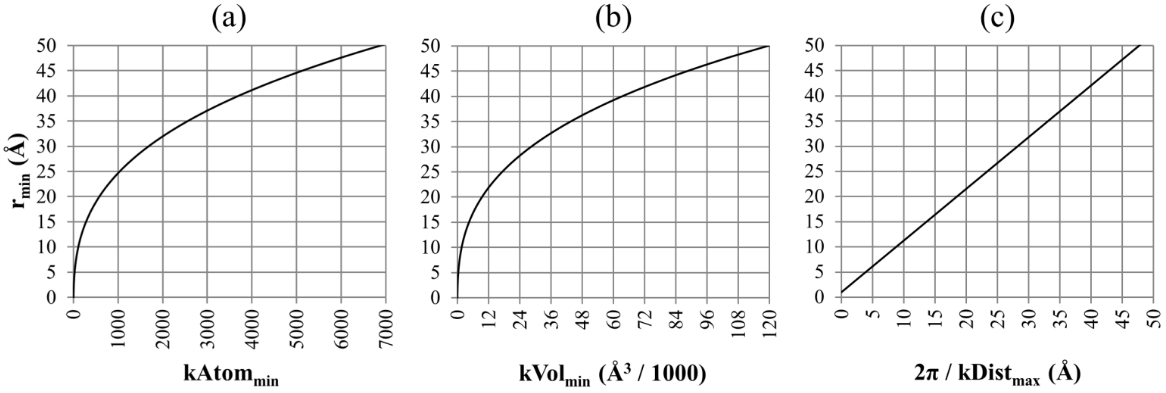

Figure 2.10. The values of r_{min} that will yield approximately the same convergence rate as three different methods for setting the minimum *k*-point density.[63]

2.5 Server framework and usage

We have made the database publicly available since early 2017. The database was made available in the form of an HTTP server with an API that takes in user input parameters in the form of a string and files which contain the structure of the material along with other necessary information to determine the symmetry of the structure. To simplify the use of the API, we provided a client-side BASH script in our website for anyone who wants to use this server.

The server was written in Java programming language and is published using the open-source Tomcat 8.0[82]. Java was chosen as the programming language due to the ease of deployment and the availability of libraries that will help with the creation of the server. The third-party libraries used were the Apache Commons[83] mainly for input/output processing, JSON for database I/O, and an open source library to deep-clone objects. The rest of the programming work was done in-house.

We chose to make the database available publicly through a server instead of an independent package due to a couple of important reasons. Firstly, is the issue of maintenance, as the database and the bulk of the algorithm exist in the server, updating and maintaining the code happens only at a single point, the server itself. In addition, a single update of the server would immediately affect the entire userbase. Secondly, the computing environment of different users vary wildly and it would be difficult to guarantee that an independent package will work for most users, especially as operating systems and software being updated frequently. By having all users access a single point through a script that will run in a BASH environment, we made sure that anyone with an internet connection will be able to use this database. Finally, the database itself takes time to load to the memory and will get better as it takes in more requests. Running the database as a server, allow the database to be pre-loaded into the memory, cutting the possible overhead cost in generating a *k*-point grid. In addition, if a more efficient grid was found while processing a request, the database will be updated with said grid and the improvement will affect the entire userbase.

The server works by first parsing in upload parameters specified through standard HTTP input format. It then processes an input file we name PRECALC, which contains specific input parameter that specifies the desired type and density of the *k*-point grid. Table 3.2 below explains the different parameters in the PRECALC file and was taken from our website (muellergroup.jhu.edu):

Parameter	**Allowed values**	**Default Value**	**Explanation**
INCLUDEGAMMA	TRUE / FALSE / AUTO	AUTO	Determines if the grid will contain the gamma point. AUTO selects the grid with the smallest number of irreducible *k*-points.
MINDISTANCE	Numeric (Angstroms)	0	The minimum allowed distance between lattice points on the real-space superlattice ($r_{\min}$ in our paper). This determines the density of the *k*-point grid.
MINTOTALKPOINTS	Numeric	1	The minimum allowed number of total *k*-points in the Brillouin zone.
KPPRA	Numeric	1	The minimum allowed number of *k*-points per reciprocal atom. We do not advise setting a value for KPPRA for systems

			with less than three periodic dimensions. For example, if KPPRA were used to set the *k*-point density for a two-dimensional slab, doubling the thickness of the slab would cut the density of the *k*-point grid roughly in half. This is probably not the desired behavior. In this case, we recommend using MINDISTANCE instead.
GAPDISTANCE	Numeric (Angstroms)	7	This parameter is used to auto-detect slabs, nanowires, and nanoparticles. If there is a gap (vacuum) that is at least GAPDISTANCE wide in the provided structure, the *k*-point density in the corresponding direction will be reduced accordingly.
REMOVE_SYMMETRY	NONE / STRUCTURAL/	NONE	An optional flag to control the symmetry operations that

	TIME_REVERSAL / ALL		reduces the *k*-point grid. The default value, NONE, will try to maximize the number of symmetry operations used to reduce the k-point grid based on the provided input files. STRUCTURAL removes all structural symmetry operations when generating the grid, retaining only time-reversal symmetry. TIME_REVERSAL removes time-reversal symmetry, retaining only structural symmetry. ALL removes all symmetry operations from consideration, so symmetry is not used to reduce the *k*-point grid.
HEADER	VERBOSE / SIMPLE	SIMPLE	Sets the verbosity of the grid information written to the file.

Table 2.2. The parameters, value, default value, and description for the server.

After obtaining the parameters that specifies the user requested grid density and type, the server processes the user uploaded structure file followed by any other file or information that may influence the symmetry of the structure. Examples of these types of information are magnetic moment specification, time-dependent calculation such as molecular dynamics, freezing of certain atoms, structures with less than three dimensions such as slabs or nanoparticle, etc. The structure and its symmetry are then processed according to said parameters and the final information of the lattice is passed on to the *k*-point database from which an appropriate grid will be generated. In the case of a problem, such as the code failing to identify the symmetry of the structure, the code will attempt to change increase its precision by a factor of two up to three times. Once the grid has been generated, it is sent to the user along with any other relevant messages. If the server was not able to generate a *k*-point grid, the user will receive a message on the reason of the failure. Currently, the server is able to process and return grid for the DFT implementation in VASP. We currently testing the capability to handle other DFT packages, such as Quantum Espresso[84, 85] and Abinit[86].

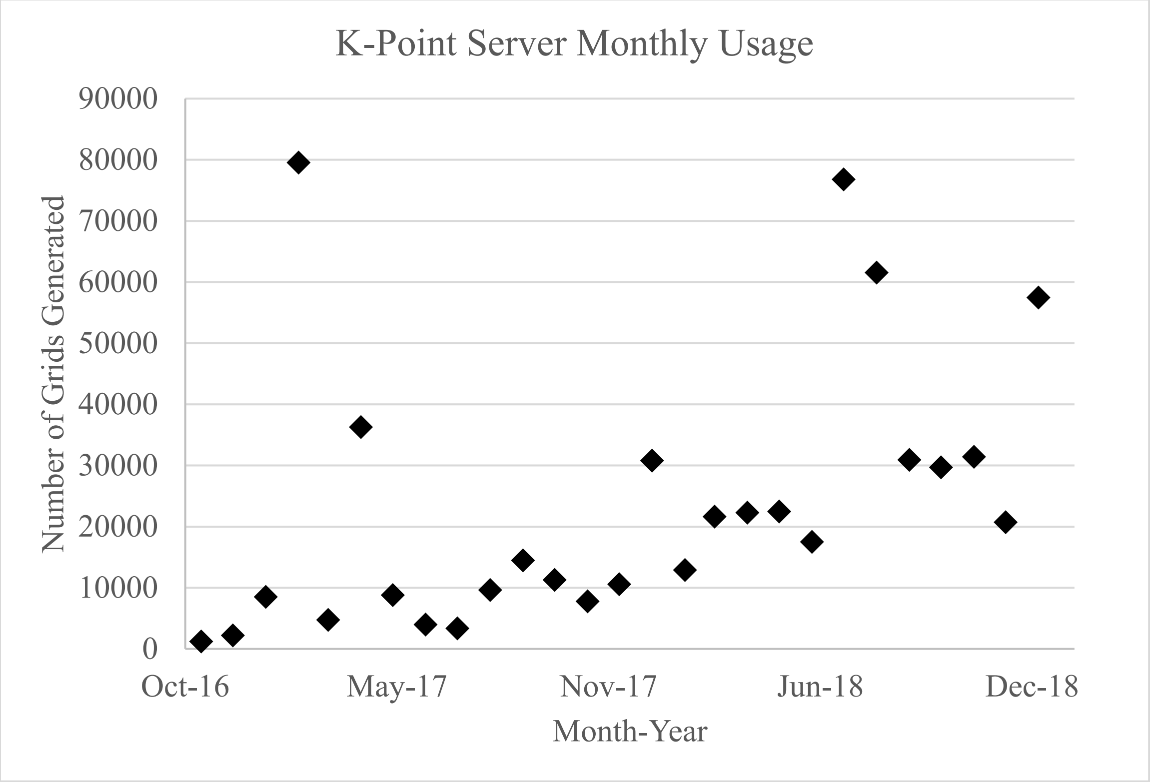

Figure 2.11 *K*-point server monthly usage statistics from October 2016 until January 2019.

As shown in Figure 2.11, the server has seen increasing usage overtime, averaging over 500 requests daily since October 2016 and has generated over 639,000 grids. We expect this trend to continue into the future.

2.6 Conclusion

We have presented a method for rapidly generating highly efficient *k*-point grids. There are several practical advantages to using the method presented in this paper. There is only one parameter, $r_{\min}$, that needs to be set by the user, and we have provided guidance on how to select a good value for this parameter. The generated *k*-point grids are always consistent with the symmetry of the material, which both preserves the symmetry of the system and maximizes the degree to which symmetry can be used to reduce the cost of the calculation. The grids are independent of the lattice vectors chosen to represent the real-space primitive cell. Thus, the user can change the way in which the structure is represented in the input file without changing the results of the calculation (at least to the extent that those results depend on the choice of *k*-points). Perhaps most importantly, grids generated using our method result in a significant reduction in the number of irreducible *k*-points required to reach a given level of convergence, resulting in large savings in computational time. For Γ-centered grids, we observed average speed-up of about 50-100% compared to a more conventional approach (Figure 2.4), and for shifted grids the speed-up is even greater. This translates to possibly hundreds of thousands of CPU hours for a given project or days for a given quantum calculation.

To allow others to generate *k*-point grids using our method, we have constructed a free and publicly available *k*-point grid server that provides access to our database of generalized *k*-point grids. This server was used to generate all GD grids in this manuscript. On average, it took 0.3 seconds to generate each of the grids for calculations converged within 1 meV / atom.

3. RAPID SCREENING FOR PROTON CONDUCTORS

3.1 Introduction to high-throughput screening for proton conductors

The main idea behind high-throughput computational or experimental approach is to discover or design a new material for a given application. The process usually involves the creation of a database followed by an intelligent enquiry of the data[31]. This idea is not new as experimentally this went back to the days of Edison[87]. However, computationally speaking only in the last two decades or so have we reached a point where the computational capabilities combined with the development of various computational tools allow this to be feasible. This was followed by efforts to create publicly available databases that contain not just structure information, but also thermodynamic information, such as Materials Project[79] and OQMD[81]. High-throughput computational approach is then become even more feasible as often times there is no more need to generate the database to screen anymore.

As mentioned in the previous chapter, there has been many computational studies on proton conductivity in oxides, with most of these studies utilizing Density Functional Theory (DFT) calculations in order to calculate the properties of the oxide[22, 25, 88-95]. However, it would take days to finish the calculation for a given structure. In order to screen a database that contains tens of thousands of oxide structures it is necessary to have a method that could check the potential for proton conductivity for a given structure within minutes. To begin, we need to identify a common descriptor, i.e. a calculatable microscopic quantity that indicates a property that is sought after. In this case, the property is proton conductivity, which occurs through diffusion process in a solid.

The rate of diffusion in solids can be described through the Arrhenius equation:

$$D = D_o \exp\left(\frac{-E_a}{kT}\right) \tag{3.1}$$

where D is the rate, D_O the rate constant, E_a the activation energy, k the Boltzmann constant, and T the temperature. This equation is typically plotted in the form of:

$$\ln(D) = \left(\frac{-E_a}{k}\right)\frac{1}{T} - \ln(D_O) \tag{3.2}$$

in order to see the influence of the activation energy with respect to temperature. Equation (3.2) then shows for most temperatures where solid phases exist that the rate would go up rapidly along with T as generally $E_a > kT$. In addition, the rise of the rate is determined by the slope of the line E_a , which signifies the importance of the activation energy as a descriptor for a good proton conductor. An example of this approach to identify the performance of a material for its protonic conductivity using an Arrhenius plot is shown in Figure 3.1.

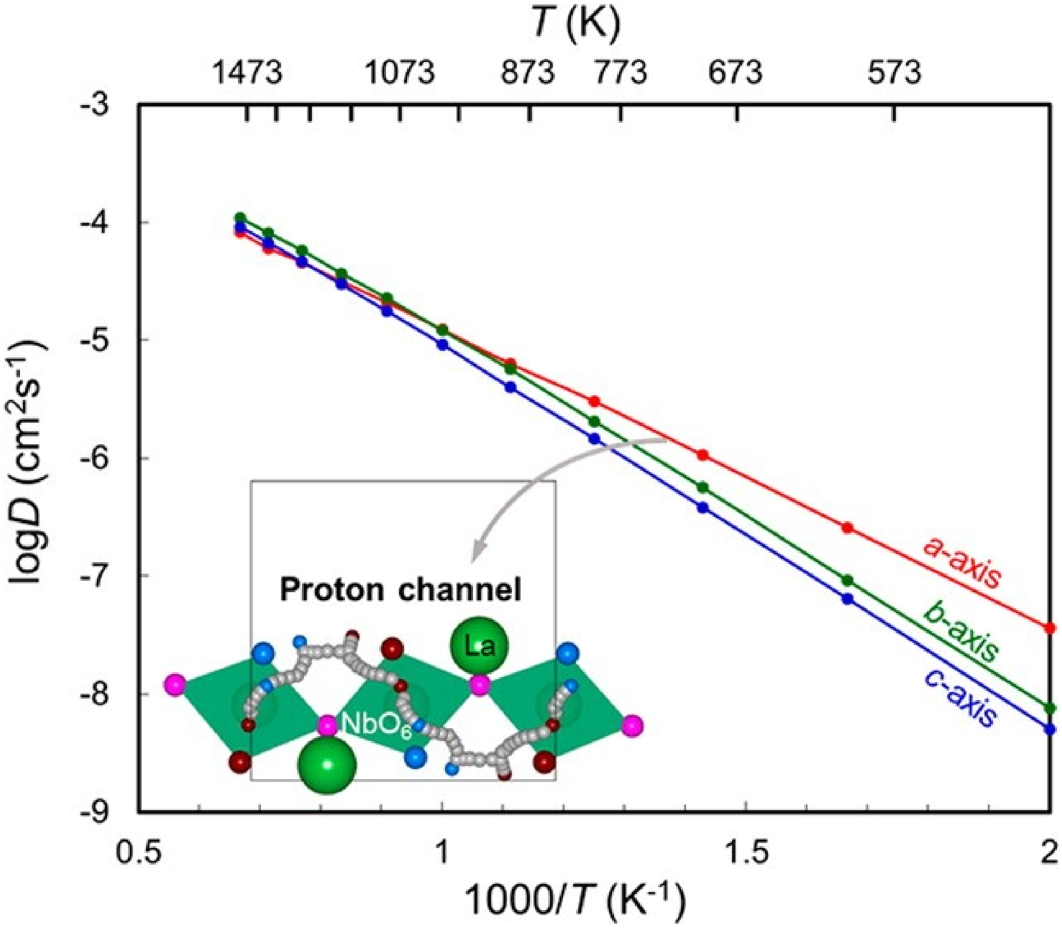

Figure 3.1 The proton conduction behavior in La_3NbO_7 is theoretically analyzed by first-principles calculations with the aid of the nudged elastic band method and the kinetic Monte Carlo method. Protons in the crystal migrate over a long range through fast conduction channels along the single NbO_6 octahedral chains in the *a*-axis direction, whose calculated potential barrier is 0.54 eV. The bridging paths connecting the proton channels in the *b*- and *c*-axes directions have a higher potential barrier, 0.64 eV, leading to anisotropic proton diffusivity and conductivity, particularly at low temperatures. The preferential bonding of protons to several specific oxide ions is strongly related to the lower potential barrier in the *a*-axis direction in addition to the presence of the infinite NbO_6 chains[96]. Figure adapted from ref. 96.

3.2 Methodology

3.2.1 Nudged Elastic Band method

The activation energy for diffusion is a kinetic property. DFT calculations are ground-state calculations, which on its own, it cannot calculate time-dependent properties. In order to calculate the transition state energy of the diffusion process an additional method is required. Nudged Elastic Band (NEB) method is an established method for finding the minimum energy path between a given initial and final state from which the activation energy can be estimated[43, 44].

The main idea behind the NEB method is to have intermediate images connected by a spring interaction forming an "elastic band" between the initial and final states. The springs would have a force with respect to the potential energy surface. By maximizing or "nudging" the force on the springs, this method can find the saddle point in the minimum energy path given. Relative to the lowest energy state from the transition process, the energy of the state on the saddle point is approximately the activation energy in a diffusion process[43-46]. Such approximation combined with DFT calculations typically have the accuracy of 0.1 eV[44, 97]. The NEB method is illustrated in Figure 3.2. It is also necessary to mention that the potential energy surface shown in Figure 3.2 is actually not "seen" by the NEB method. The NEB method only recognizes the energy of the intermediate images.

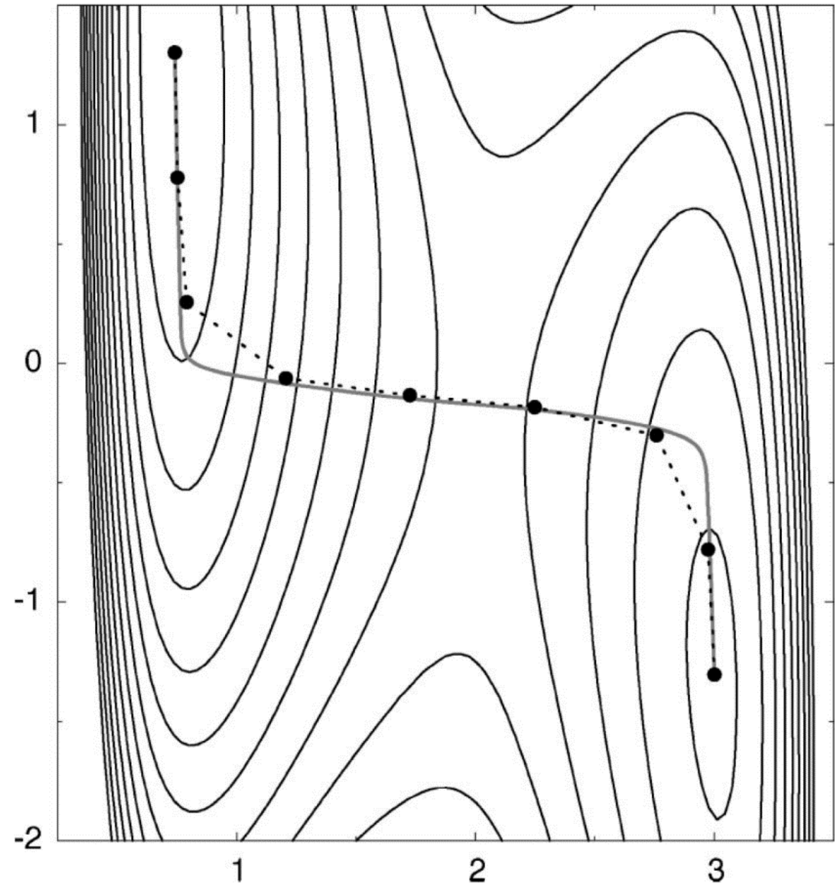

Figure 3.2. An illustration of the NEB method. The dotted lines connect the images and the solid line represent the overall pathway.[43] . Figure adapted from ref. 50.

Climbing image nudged elastic band (CI-NEB) is a variant of the NEB method where a standard NEB method is done to identify the image that could possibly be the saddle point followed by removing the one image at the saddle point from the spring forces. The other images are then used as reference points for the removed image. The removed image then has a different force component applied which, qualitatively, would lead it moved up the potential energy surface along the elastic band and down the potential surface perpendicular to the band. In effect what this does is ensuring that the image at the saddle point is actually at the transition state. In addition, as shown in Figure 3.3, the images adjacent to the saddle image will be pushed closer to the location of the saddle point, allowing a more accurate approximation of the saddle point energy. The NEB method utilized in this thesis is the CI-NEB, with the application made as a separate additional package for VASP[98].

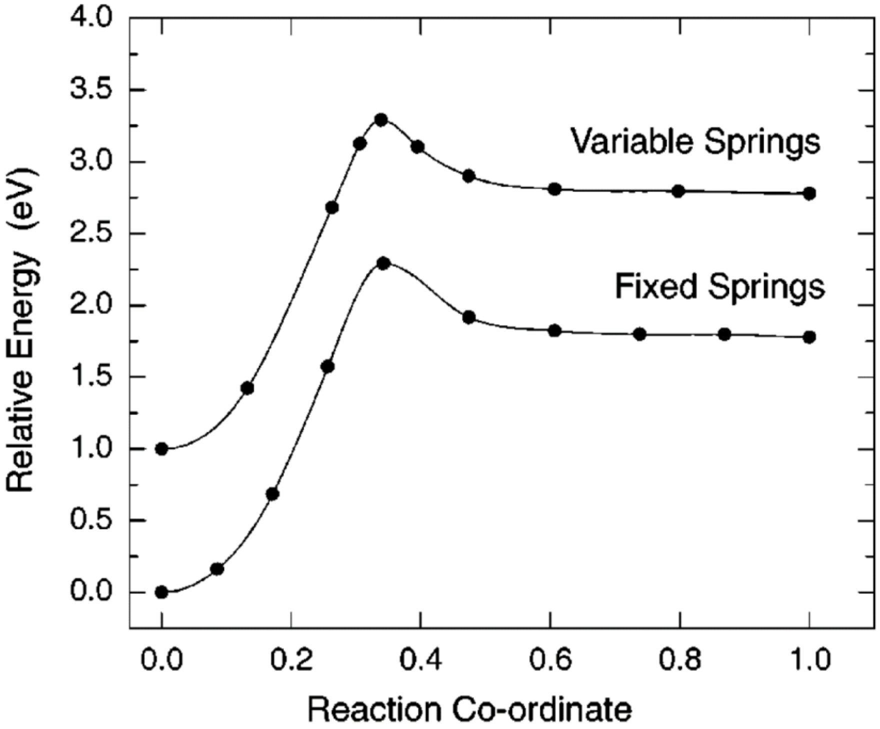

Figure 3.3. Density functional theory calculations of the minimum energy path for H2 dissociative adsorption on a Si~100 surface. The H adatoms sitting on adjacent Si atoms in a surface dimer correspond to reaction coordinate of 0.0. The H2 molecule 3.8 Å away from the surface corresponds to 1.0. A regular climbing image NEB calculation with equal spring constants ~curve labeled ‘‘Fixed Springs’’ is compared with a calculation where the spring constants are scaled with the energy ~curve labeled ‘‘Variable Springs,’’ arbitrarily shifted by 1.0 eV. Both calculations involve 8 movable images. The variable spring calculation results in a higher resolution of the barrier with insignificant additional computational effort.[98]. Figure adapted from ref. 76.

3.2.2 Energy Model

The model used for screening in this work is based on a combination of exponential repulsion and screened Coulomb potential. The screened Coulomb potential represents the electrostatic interaction that occurs in this ionic environment. The screening effect is there because of the fact that these interactions are short-range interactions with the positive nucleus shielded by the electrons around it, making the electrons not as strongly bounded. The exponential repulsion term represents a typical pair-potential bond, where the two atoms will experience an exponentially repulsive force as they get closer, but still allows bond breaking as they get sufficiently far apart. The energy for a given pair of atoms in a solid is then:

$$E_{pair} = E_{Exp} + E_{Coulomb} \tag{3.3}$$

where $E_{Coulomb}$ is the screened Coulomb potential:

$$E_{Coulomb} = k\frac{q_i q_j}{r}\exp\left(-\frac{r}{d}\right) \tag{3.4}$$

with k as the Coulomb constant, q the charge of the two atoms, r the distance between the two atoms, and d the screening radius. E_{Exp} represents the exponential repulsion, which is:

$$E_{Exp} = A\exp\left(-rC\right) \tag{3.5}$$

where r is the distance between two neighboring atoms, and both A and c are constants for specific element pairs based on the bond-valence theorem parameters by O'Keefe and

Brese[99]. The bond-valence theorem itself relates the sum of valences for a given atom to their bond distances:

$$s_{ij} = \exp\left(\frac{R_o - r}{b}\right) \tag{3.6}$$

with s_{ij} representing the valence between bond of atom I and j, r the distance between the two atoms, and b is the universal bond-valence parameter with the value of 0.37A. R_o is the bond valence parameter for the given pair of atoms and is determined using the value from O'Keefe and Brese's paper with the formula:

$$R_o = r_i + r_j - \frac{r_i r_j (\sqrt{c_i} - \sqrt{c_j})^2}{c_i r_i + c_j r_j} \tag{3.7}$$

where r and c are element-specific parameters listed in their paper. We then optimize the parameters A and c in equation (3.7) for a given species on the structures of zincblende, rhenium trioxide, cristabolite, cuprite, wurtzite, rutile, fluorite, rocksalt, and cesium chloride using a conjugate gradient routine. This process is described in Figure 3.4 below.

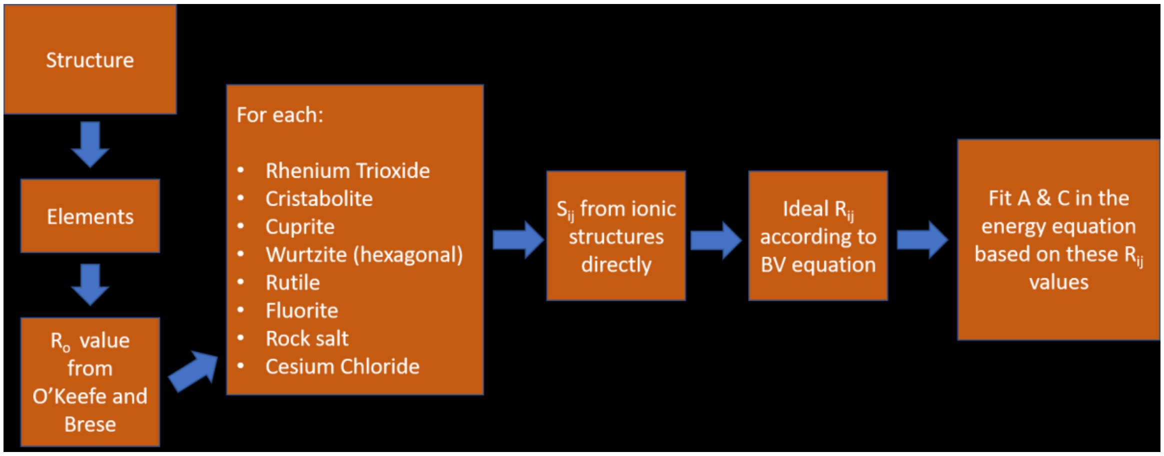

Figure 3.4. The process in having the BV method expressing the energy of a bond through the A and c parameters in the exponential term.

There are a few important reasonings behind the selection of BV method for the energy model. The first and most important is that the BV method is well parametrized for most elements in the periodic table[51]. In addition, there are multiple forms describing the BV parameter depending on what those parameters were used for and what they were fitted on that we were able to consider[48, 99]. While the BV method is empirical, it has been shown to work very well for ionic systems, which are the systems studied in this chapter[51]. Finally, the combination of the BV method and the energy model as shown in equation 3.4 and 3.5, has three parameters to fit, A, c, and d which ensures that they could be fit well without requiring thousands of training data.

3.2.3 Treatment of solids and relaxation

To take into account the possible relaxation of atoms in the solids, we treat the solids as Einstein solids, that is the atoms in a given solid would vibrate at the same frequency and each one of them are independent quantum harmonic oscillator.

When the diffuser is inserted to the atom this is then taken into account by the energy as the atoms around it are displaced. With $E_{pair}(r)$ as the energy from the pair of atoms and $E_{relax}(r)$ as the energy taking account of the displacement:

$$E_{relax}(r) = E_{pair}(r + r_{offset}) + \frac{k}{2}(r_{offset})^2 \tag{3.8}$$

we then have r representing the ideal distance between the atoms, k the spring constant, and r_{offset} the offset distance taking into account the displacement.

To find the value of r_{offset} at equilibrium, the force between the two atoms must be zero:

$$0 = \frac{dE_{relax}(r)}{dr_{offset}} = E_{pair}'(r + r_{offset}) + 2kr_{offset} \tag{3.9}$$

from which $E_{pair}'(r + r_{offset})$ we approximate using Taylor expansion:

$$E_{pair}'(r + r_{offset}) \approx E_{pair}'(r) + E_{pair}''(r)r_{offset} \tag{3.10}$$

substituting equation (3.9) back to equation (3.10):

$$0 = \frac{dE_{relax}(r)}{dr_{offset}} = E_{pair}'(r) + E_{pair}''(r)r_{offset} + kr_{offset}$$

$$0 = E_{pair}'(r) + r_{offset}\left(E_{pair}''(r) + k\right)$$

$$r_{offset} = \frac{-E_{pair}'(r)}{E_{pair}''(r) + k} \tag{3.11}$$

with this we have taken into account the displacement that occurs when the hydrogen diffuser is in the solid oxide system.

3.2.4 Mapping diffusion pathways and finding minimum energy pathway

This simple energy model then allows us to create a map of potential energy surface by creating grid points over the lattice of the structure. By taking the derivative of the energy equation, we have:

$$\frac{dE_{pair}}{dr}=\frac{dE_{Exp}}{dr}+\frac{dE_{Coulomb}}{dr} \tag{3.12}$$

$$\frac{dE_{pair}}{dr}=-AC\exp\left(-rC\right)-\left(\frac{1}{d}+\frac{1}{r}\right)\left(k\frac{q_iq_j}{r}\exp\left(-\frac{r}{d}\right)\right) \tag{3.13}$$

By taking the partial derivatives with respect to the axes, we can obtain the gradient of the potential energy surface. Similarly, by taking the second derivative:

$$\begin{aligned}\frac{d^2E_{pair}}{dr^2}&=AC^2\exp\left(-rC\right)\\&+\left(\begin{array}{l}\left(-\frac{1}{d}-\frac{1}{r}\right)\left(\frac{1}{d}+\frac{1}{r}\right)\left(k\frac{q_iq_j}{r}\exp\left(-\frac{r}{d}\right)\right)\\+\frac{1}{r^2}\left(\frac{1}{d}+\frac{1}{r}\right)\left(k\frac{q_iq_j}{r}\exp\left(-\frac{r}{d}\right)\right)\end{array}\right)\end{aligned} \tag{3.14}$$

and then taking the partial derivatives with respect to the axes, we will obtain the hessian matrix of the potential energy surface.

Combining the information from equation (2.18) and equation (2.19), we can algorithmically find the stable sites and the saddle points. Connecting the stable sites through the saddle points by a linearly interpolated vector adjusted to the potential energy surface will generate a map of overall possible diffusion pathways. The minimum energy pathway would then be a combination of diffusion hops in the map that goes through the entire unit cell that has the lowest energy difference between the saddle point with the highest energy and the stable site with the lowest energy, i.e. the activation energy of the minimum energy pathway.

3.3 DFT calculations and activation energy calculation with the CI-NEB method

3.3.1 Material selection

We began our selection of materials to study from ABX_3 cubic perovskites as they represent the structure type that is studied the most for proton conductivity. In addition, the high symmetry in cubic perovskites make the number of possible diffusion hops to be small and the overall diffusion pathway map to be easy to understand. Using the book by Muller and Roy[100] as reference, we then expanded the study to another ABX_3 family, hexagonal perovskites. The A_2BX_4 spinel which has increased complexity was studied next. To add another layer of complexity we added A_2BCX_6 elpasolite structure type. Finally, we add some additional oxides taken from Roy and Muller. The list of all materials calculated using the NEB method is listed in table x. All structure files were taken from ICSD[73]. In total there are 52 total oxides structures evaluated, with 18 cubic perovskite structures, 5 hexagonal perovskite structures, 15 spinel structures, 8 elpasolite structures, and 6 structures from various structure types.

3.3.2 DFT calculations

All DFT calculations were done with VASP[65-69] software package version 5.3. The crystal structure files from the ICSD[73] database were first converted into a primitive cell in the format for VASP. To ensure our energy model and the following NEB calculation to process the same structure, we only relax the lattice parameters of the structures, keeping their atomic positions untouched. The electronic minimization was done using a combination of blocked Davidson iteration scheme and RMM-DIIS[101, 102].

Perdew-Burke-Ernzerhof (PBE)[103] projector augmented wave (PAW)[74] pseudopotentials were used for all calculations. Energy precision for the pseudopotential and FFT grid was set to a high value using the parameter “accurate”. To take into account of possible spin polarization in the material, all calculations are set to be spin polarized. The self-consistency cutoff was set to 10^{-5} and the relaxation cutoff was set to 10^{-3}. The relaxation was done using the RMM-DIIS algorithm.

The *k*-point grid was generated using the generalized Monkhorst-Pack grids[63], which is explained in Chapter 2. The minimum periodic distance chosen was 28.1 Angstroms which is sufficient to ensure energy convergence for non-metals with the Γ point centering set to automatic, depending on which grid has less number of symmetrically irreducible *k*-points[63].

3.3.3 Activation energy calculation with NEB method

In calculating the activation energy, firstly a supercell was made out of the primitive structure file with a periodic distance of 8 Angstroms. To ensure consistency to the placement of the hydrogen atom in the supercell between the energy model and DFT calculation, the supercell was first made with the original input file whose lattice vectors then resized according to the change in lattice vector of the relaxed primitive cell.

After the hydrogen atom has been placed in the supercell sites, the intermediate images for the NEB calculation was made with a distance of 0.5625 Angstroms between each other. The end points of the NEB calculation had their lattice vector frozen and atomic positions relaxed. The relaxation process used the same parameters as the primitive cell calculation with several differences.

One aspect that we would like to take into account is that compared to most transition metals that is used as a part of the ceramic compound, hydrogen is often more electropositive[104]. This means that instead of having a diffusing proton in the solid, there will a diffusing a hydrogen atom which carries no charge. To guarantee that the hydrogen atom is acting as a proton, a single electron was removed.

Next, based on the primitive cell calculation, the spin values for the supercell calculations were set. The relaxation algorithm was also changed to conjugate gradient. Finally, the self-consistency cutoff was increased to 10^{-6} and relaxation cutoff was reduced to 10^{-2}. As noted by Sundell et al., it is important to allow the atoms to relax as surroundings of the protons distort during the transition and shorten the distance that the proton has to hop from, as shown in Figure 3.5[92]. If the ions other than the hydrogen are not allowed to move, the resulting energy will become artificially high and thus inaccurate, as what Munch et al. calculated[26].

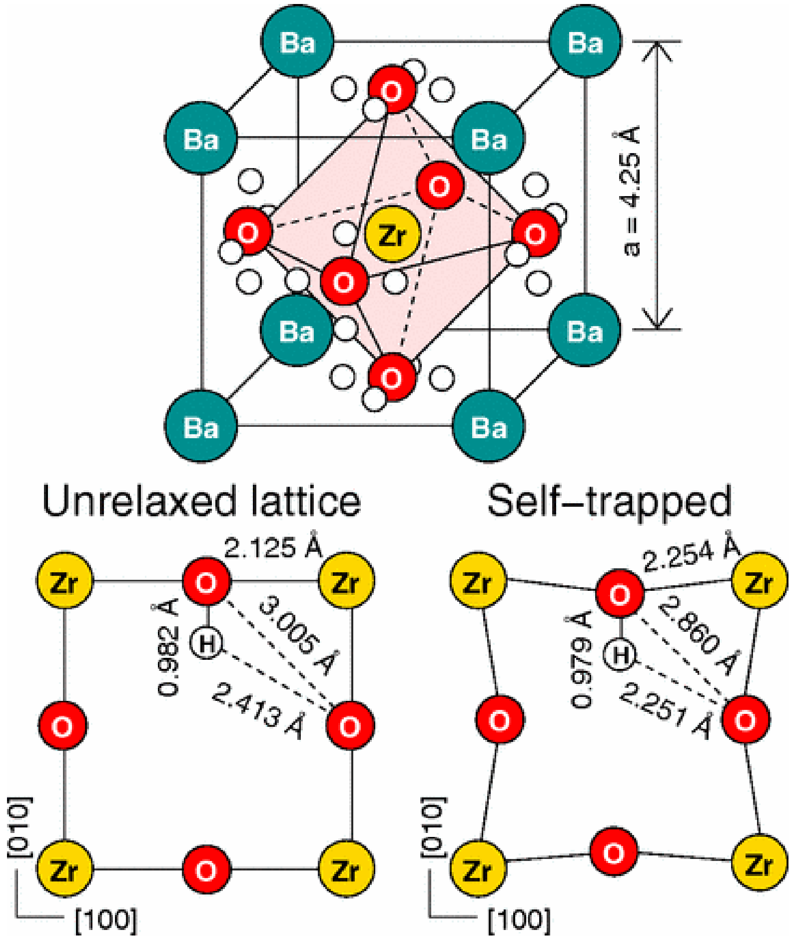

Figure 3.5 The equilibrium position for a hydrogen interstitial in $BaZrO_3$ (calculated lattice parameter a_0=4.25Å) is close to an oxide ion, with the O-H distance equal to 0.98Å and the O-H axis oriented along the bisector of two oxygen-oxygen connecting lines. The protonic defect interacts strongly with the host lattice, which is manifested as a large self-trapping distortion of the positions of the surrounding atoms[92]. Figure adapted from ref. 66.

The NEB calculation itself used the CI-NEB method developed and implemented by the Henkelman group[43-46, 98]. The spring value used for the elastic band was 5 and the optimization algorithm used was damped molecular dynamics with step size of 0.01.

3.3.4 Database processing

We began by looking through the entire ICSD database and removing structures that do not contain oxygen. This presented us with over 37,000 structures to work with. These structures are then grouped by their space group number as listed in their CIF files by ICSD. To ensure no structures were double counted we checked for their uniqueness. Checking for structure uniqueness was not a trivial process as one has to compared not only the type and number of elements, but also symmetry and the possibility that a structure might be oriented differently or is a supercell of the other.

After the structures have been checked for their uniqueness, they are grouped by their respective structure types which gave us 3,663 different oxide families. As most of these families contain very small number of members, we decided to focus on families with members of at least 20 structures. This step left us with 41 different structure types consisting of 1946 structures in total. The preprocessing described here is depicted in Figure 3.6.

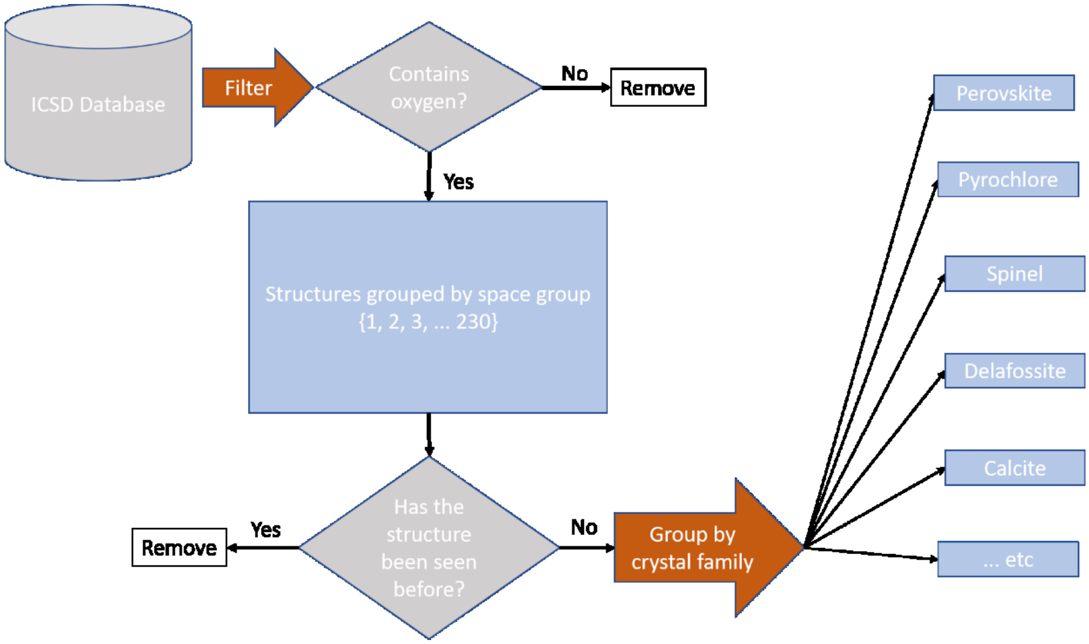

Figure 3.6 The framework describing the database preprocessing and sorting steps.

3.4 Prediction of activation energy

Using the energy model and its associated frameworks described in the methodology, we predicted the activation energy for the cubic perovskite structure type. We then used the results to improve the model parameters and used it to predict the hexagonal perovskite family, we then repeat the process with spinel, elpasolite, and several other randomly selected structures. The result of the model fitted with all 52 structures is shown in Figure 3.7 below.

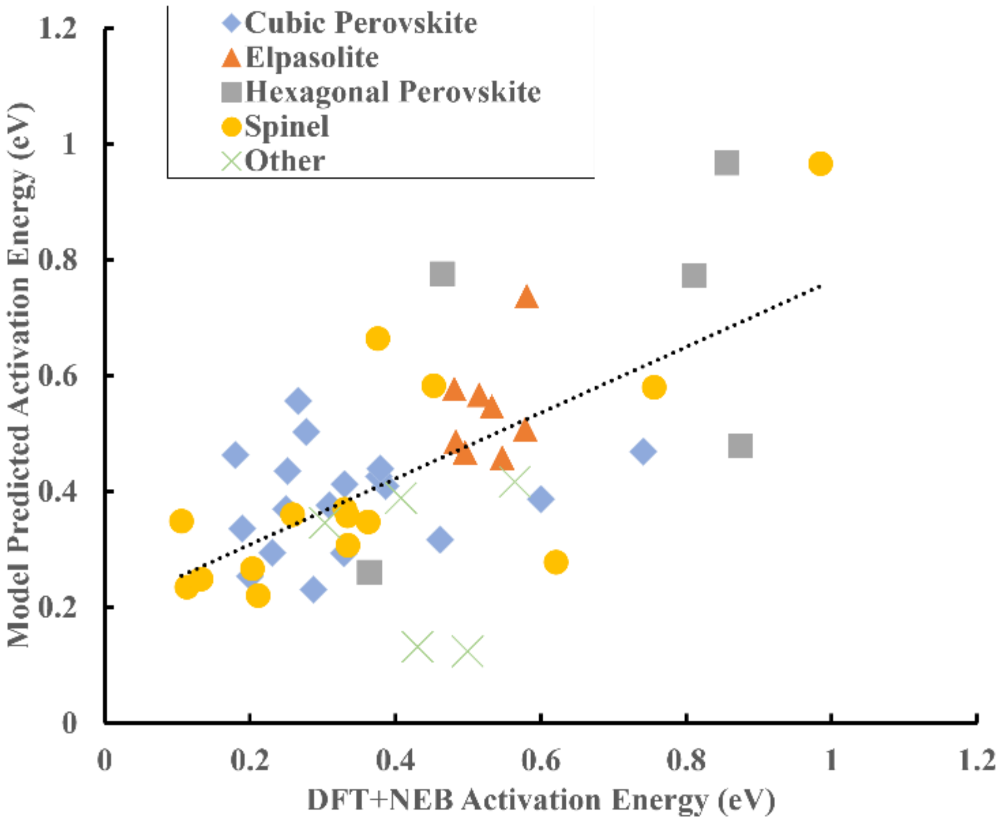

Figure 3.7 A plot of activation energy calculated by DFT+NEB vs. predicted by the energy model. Blue diamonds represent cubic perovskites, orange triangles represent elpasolites, grey squares represent hexagonal perovskites, yellow circles represent the spinel structure type, and structure types with less than 5 members in the dataset are put together and represented by the green cross. The dotted line is a linear trendline representing all the data in the plot.

As Figure 3.7 shows, the overall trend of in the comparison between DFT+NEB energy and the energy predicted by the model is quite linear and it resembles Figure 1.3. in which there is a sizeable deviation from a linear fit.

The average of the difference between the two methods is 0.126 eV, which is quite large. To minimize the noise in the dataset, we took the average energy for a given oxide structure type in our dataset which has at least 5 structures.

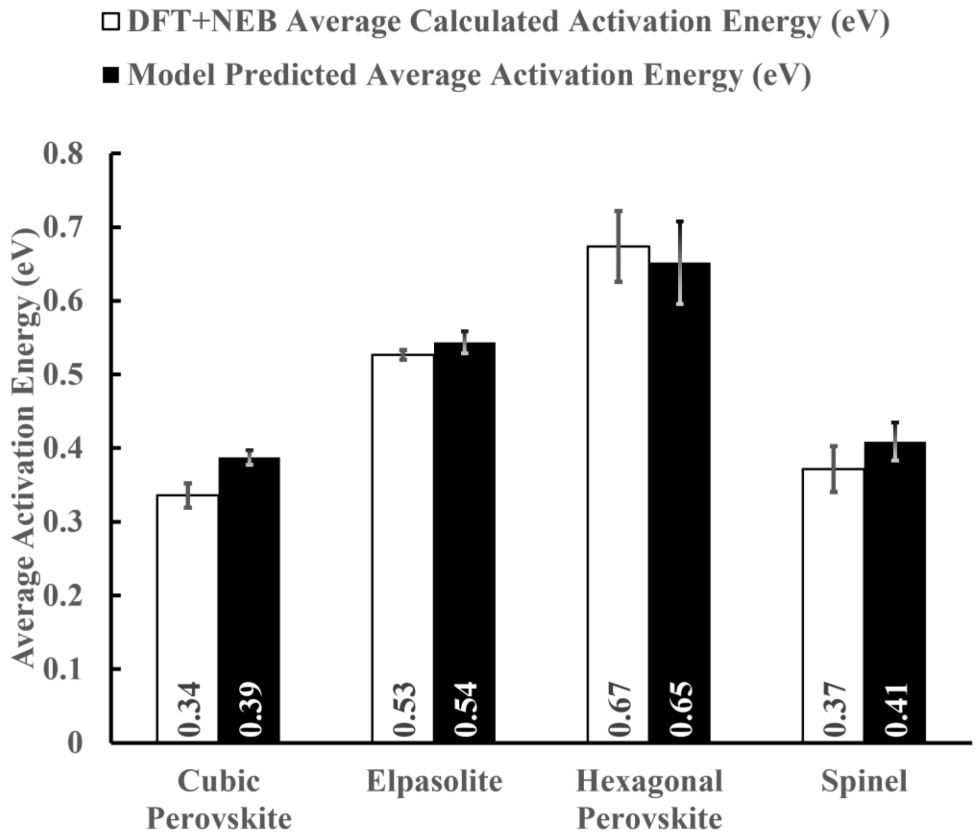

Figure 3.8 Average activation energy for DFT+NEB and the energy model.

As we can see in Figure 3.8, significant noise was removed when the average of the activation energy was taken. The average error from the energy model for the prediction of the activation energy for structure types is 0.0320 eV, which is below the error from the approximation of activation energy with the DFT+NEB, which is in the order of 0.1 eV.

Composition	Oxide Structure Type	Model Predicted Activation Energy (eV)	DFT+NEB Calculated Activation Energy (eV)	Absolute Difference (eV)
Ca_2MgWO_6	Alternating Perovskite	0.416737	0.564008	0.147271
$CrSrO_3$	Cubic Perovskite	0.25348	0.19972	0.053759
$CaTiO_3$	Cubic Perovskite	0.317002	0.46147	0.144468
$MoSrO_3$	Cubic Perovskite	0.386586	0.599814	0.213228
$KTaO_3$	Cubic Perovskite	0.409248	0.386502	0.022745
$GePbO_3$	Cubic Perovskite	0.293683	0.3292	0.035517
$CaSiO_3$	Cubic Perovskite	0.426016	0.37739	0.048626
$NaWO_3$	Cubic Perovskite	0.294477	0.230381	0.064096
$KCrO_3$	Cubic Perovskite	0.375982	0.309166	0.066816
$SrZrO_3$	Cubic Perovskite	0.469067	0.741086	0.272019
$BaTiO_3$	Cubic Perovskite	0.369738	0.249483	0.120255
$BaZrO_3$	Cubic Perovskite	0.502707	0.27732	0.225387
$BaIrO_3$	Cubic Perovskite	0.439164	0.378972	0.060192
$BaSnO_3$	Cubic Perovskite	0.463129	0.179522	0.283607
$BaPbO_3$	Cubic Perovskite	0.556238	0.266042	0.290196
$SrNbO_3$	Cubic Perovskite	0.412975	0.330074	0.082901
$BaNbO_3$	Cubic Perovskite	0.435342	0.251341	0.184001
$LaAlO_3$	Cubic Perovskite	0.230819	0.287421	0.056601
$SrTiO_3$	Cubic Perovskite	0.335922	0.189221	0.1467
$Ba_2NiO6Re$	Elpasolite	0.737628	0.580371	0.157257

GaO_6SbSr_2	Elpasolite	0.567261	0.514962	0.052299
Ba_2MgWO_6	Elpasolite	0.546621	0.532571	0.01405
Ba_2FeMoO_6	Elpasolite	0.507778	0.578513	0.070736
Ba_2FeReO_6	Elpasolite	0.458289	0.546507	0.088218
Ba_2ZnReO_6	Elpasolite	0.486157	0.48288	0.003277
Ba_2CoReO_6	Elpasolite	0.577129	0.480684	0.096445
Ba_2MoNiO_6	Elpasolite	0.467585	0.495648	0.028063
$BaSiO_3$	Hexagonal Perovskite	0.479127	0.87437	0.395243
$BaNiO_3$	Hexagonal Perovskite	0.773659	0.810901	0.037242
$BaRuO_3$	Hexagonal Perovskite	0.776816	0.464395	0.312421
$BaCoO_3$	Hexagonal Perovskite	0.968349	0.855273	0.113075
$LaCrO_3$	Hexagonal Perovskite	0.26082	0.363617	0.102797
$Si_2Sc_2O_7$	Pyrocholre	0.388962	0.40772	0.018758
SiO_2	Quartz	0.123985	0.499558	0.375574
Rh_2ZnO_4	Spinel	0.369029	0.330071	0.038958
Rh_2MgO_4	Spinel	0.360327	0.258765	0.101562
Rh_2CoO_4	Spinel	0.357971	0.333853	0.024119
Ni_2SiO_4	Spinel	0.234994	0.112817	0.122177

Al_2MgO_4	Spinel	0.249057	0.132738	0.116319
Rh_2CdO_4	Spinel	0.580161	0.756126	0.175965
$MgTi_2O_4$	Spinel	0.277899	0.620978	0.343079
CdV_2O_4	Spinel	0.582393	0.452657	0.129736
$GeCo_2O_4$	Spinel	0.266736	0.203161	0.063575
Cr_2CdO_4	Spinel	0.347283	0.362269	0.014986
$CdIn_2O_4$	Spinel	0.664341	0.375366	0.288975
$AlNi_2O_4$	Spinel	0.967221	0.984806	0.017585
$ZnAl_2O_4$	Spinel	0.220391	0.210962	0.00943
Mg_2VO_4	Spinel	0.348982	0.105376	0.243606
Ga_2ZnO_4	Spinel	0.307155	0.334726	0.027571
$CaFeO_3$	Tilted Perovskite	0.345664	0.30236	0.043304
$BaNbO_2$	Zircon	0.131521	0.430281	0.298761

Table 3.1. All 52 structures used to fit the energy model, along with their structure types, DFT+NEB activation energy, energy model predicted activation energy, and absolute difference.

Cubic perovskites, being the most studied proton conductor, as expected has a relatively low activation energy. The DFT+NEB activation energy values for $BaZrO_3$, $BaTiO_3$, $SrTiO_3$, and $SrZrO_3$ are comparable to the study by Bork et al[25]. It is interesting that the value for cubic and hexagonal perovskite to be very different even though they share the same composition of ABX_3. This implies that the structure type plays a big role in determining the activation energy.

In Figure 3.8 we also observe that the spinel structure type has a similar activation energy value with cubic perovskites. As we can observe from Figure 3.7 and looking at the values in Table 3.1, some members of the spinel family have lower activation energy for proton diffusion than cubic perovskites. This indicates that the spinel crystal class might be worth an additional study as a possible fast proton conductor.

3.5 Minimum energy pathways

On top of the activation energy for proton diffusion, it is also important to note the actual minimum energy pathway. Do note that the full paths from the energy model include all possible pathways according to the energy model and not just ones related the minimum energy pathways. All figures in this section were made with VESTA[105].

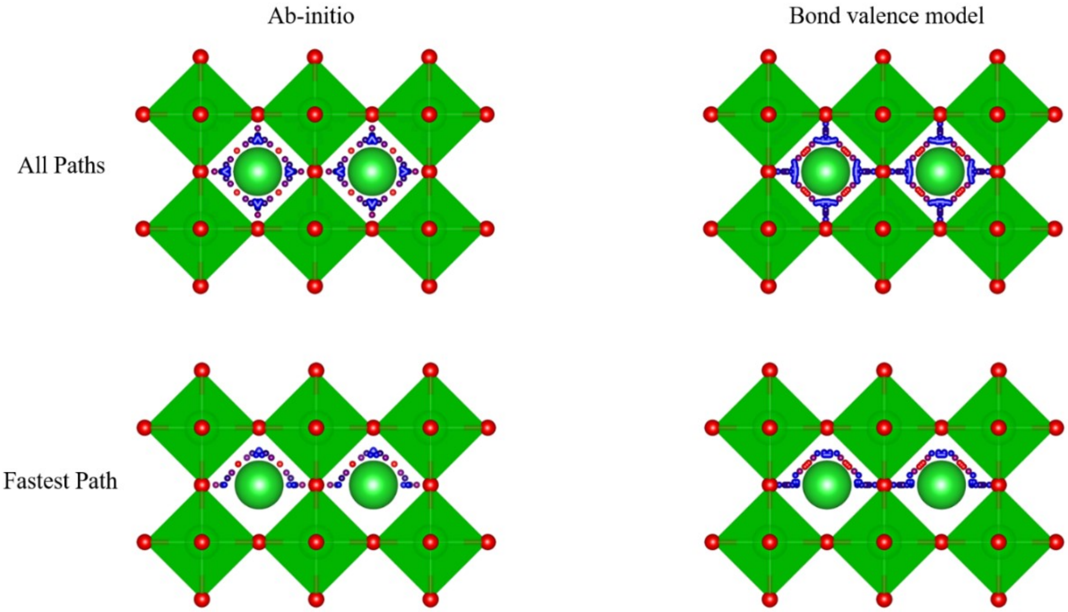

Figure 3.9 All diffusion paths and fastest diffusion paths for $BaZrO_3$, which is one of the members of the cubic perovskite crystal class. Green spheres represent barium, green octahedra represent ZrO_6 with red spheres represent oxygen. Small blue and red spheres represent the diffusion pathway, with blue indicating low energy sites and red indicating high energy sites.

Figure 3.9 shows the diffusion pathway cubic perovskite, which is represented by $BaZrO_3$. As we can see, the energy model pathways correspond well to DFT+NEB pathways. In addition, we can clearly see the Grotthuss mechanism, where the proton rotates around the oxygen atom before hopping to the next oxygen atom. While the trend might vary for different perovskite structures, it is also notable that the longer hop, from one oxygen to the next, is the bottleneck of the diffusion, as it is typically.

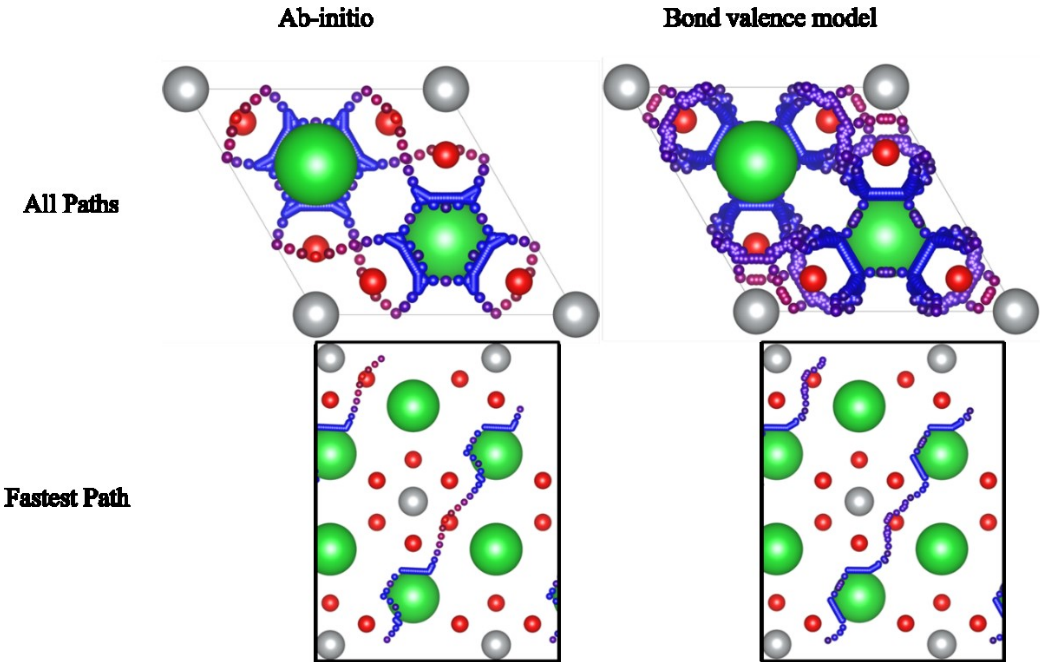

Figure 3.10 All diffusion paths and fastest diffusion paths for $BaNiO_3$, which is one of the members of the hexagonal perovskite crystal class. Green spheres represent barium, silver spheres represent nickel, and red spheres represent oxygen. Small blue and red spheres represent the diffusion pathway, with blue indicating low energy sites and red indicating high energy sites.

As mentioned in the previous section, despite having the same type of composition, ABX_3, hexagonal perovskite structure type has significantly higher activation energy on average. Looking at the fastest path shown in Figure 3.10, we can deduce the cause. Hexagonal perovskite also has Grotthuss mechanism observable and with the same trend as cubic perovskite, where the hop from one oxygen to the next is the bottle neck. However, as we can see from Figure 3.5, in the cubic perovskite $BaZrO_3$, the distance hydrogen has to travel from one oxygen to the next is roughly 2.8 angstroms, on the other hand in the hexagonal perovskite $BaNiO_3$ that distance is roughly 3.6 angstroms. As the shape of the minimum energy pathway is similar for all members for a given structure types, this additional distance in oxygen-oxygen hop would explain the higher activation barrier in hexagonal perovskites.

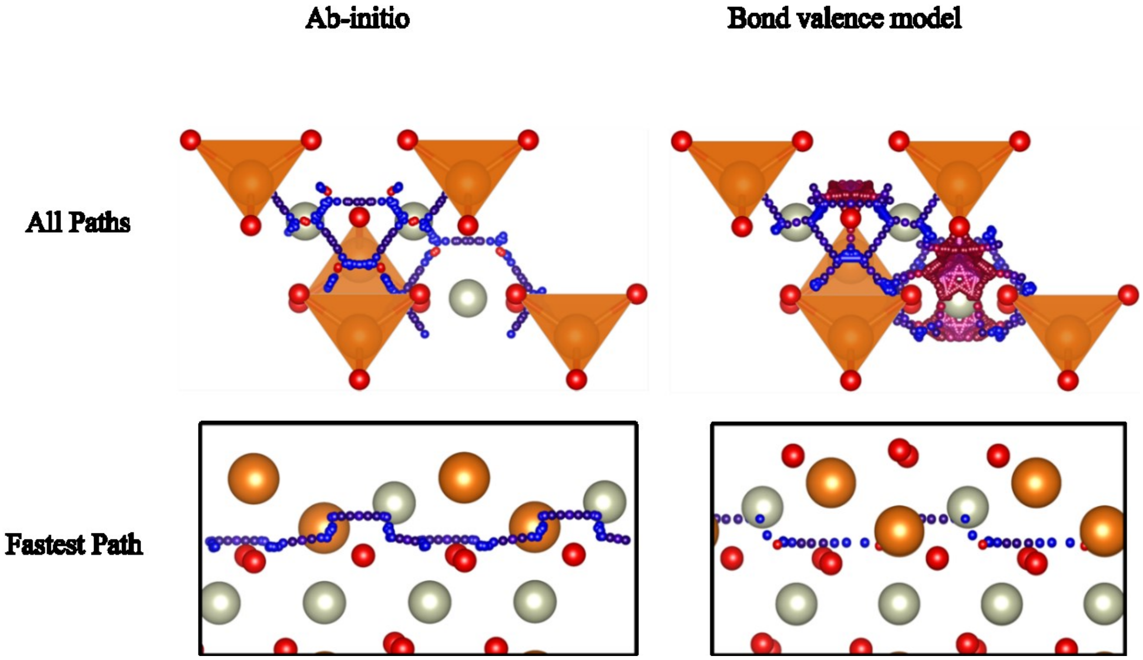

Figure 3.11 All diffusion paths and fastest diffusion paths for Rh_2MgO_4, which is one of the members of the spinel crystal class. Silver spheres represent rhenium, orange spheres represent magnesium, and red spheres represent oxygen. Small blue and red spheres represent the diffusion pathway, with blue indicating low energy sites and red indicating high energy sites.

As mentioned in the section above, spinel structure type on average has activation energy that is comparable to the cubic perovskites. However, there has been minimal number of studies of spinel as a proton conductor. The experimental study by Fukatsu et al. on $MgAl_2O_4$ established that hydrogen atom would act as a proton inside the spinel[106]. In addition to this spinels are already used for other purposes, such as catalyst for ORR and its method of synthesis are widely known[107]. It would then be very interesting and worthwhile to experimentally test the spinel structure type for its proton conductivity.

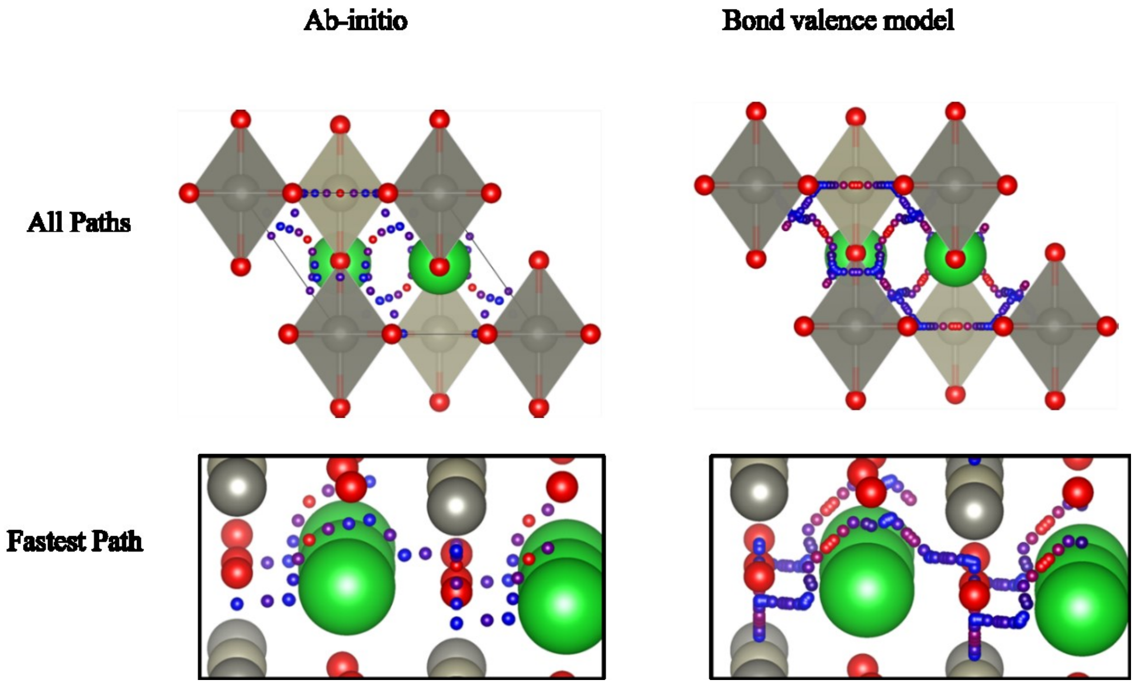

Figure 3.12 All diffusion paths and fastest diffusion paths for Ba_2ReZnO_6, which is one of the members of the elpasolite crystal class. Silver spheres represent rhenium, grey spheres represent zinc, green spheres represent barium, and red spheres represent oxygen. Small blue and red spheres represent the diffusion pathway, with blue indicating low energy sites and red indicating high energy sites. Note that the diffusion hop around the oxygen between ab-initio results and the energy model are mirror image of each other, but otherwise equivalent.

Elpasolite was added to the data set as a step up in complexity as it is a quaternary oxide. There have not been many works on the elpasolite structure type, with less than two dozen publications published yearly from 1948, totaling to 458 in 2018. Recent studies on the elpasolite structure type are testing the possibility of using it as a semiconductor[108]. However as a case study, we showed that our model was able to predict the activation energy of the relatively complex elpasolite structure type quite accurately, along with its diffusion pathways.

3.6 Ranking the oxide structure types

Extending the energy model to the processed ICSD database as mentioned in section 3.3.4, we can have the average activation energy for the entire population of the structure type. This comparison is shown in Table 3.2.

Oxide Structure Type	**Model Predicted Average Activation Energy – Sample (eV)**	**DFT+NEB Average Calculated Activation Energy – Sample (eV)**	**Model Predicted Average Activation Energy – Population (eV)**
Cubic Perovskite	0.3873	0.3358	0.4320
Elpasolite	0.5436	0.5265	0.6919
Hexagonal Perovskite	0.6518	0.6737	0.6807
Spinel	0.4089	0.3716	0.3587

Table 3.2. The average activation energy from the sampled model for the four structure types shown in Figure 3.8 along with the predicted activation energy for the entire population.

The average activation energy for the entire structure type difference with the sampled DFT+NEB activation energy is within 0.1 eV for cubic perovskite, hexagonal perovskite, and spinel. At 0.17 eV, the difference for the elpasolite structure type is larger, which might have been caused by the fact that the elpasolite structure type has one of the highest number of members (140) in contrast to the number of samples for this structure type. However, for a screening method, we believe this difference is within an acceptable range.

Using the energy model, we ranked all oxide structure types with members larger than 20. On average, predicting the average activation energy for a structure type takes around 20 minutes in a single core, which is only a small fraction of the cost of DFT+NEB calculation. These results are shown in Table 4.3.

Rank	**Average Activation Energy (eV)**	**Average Activation Energy Prediction Time (s)**	**Structure Type Name (according to ICSD)**	**Number of Members**
1	0.1935	880.58	$CrVO_4$	29
2	0.3116	652.78	Calcite	20
3	0.3258	915.22	Zircon	64
4	0.3324	1003.51	$NaMn_7O_{12}$	32
5	0.3331	493.76	$YNbO_4$(mS24)	27
6	0.3587	1093.26	Spinel - Al_2MgO_4	64
7	0.3645	491.08	Rutile	43
8	0.3821	673.09	$LiYb(WO_4)_2$	30
9	0.3907	1486.32	Pyrochlore	113
10	0.4023	831.24	Scheelite	46
11	0.4214	1006.57	ZrCuSiAs - $CuHfSi_2$	61
12	0.4320	167.66	Cubic Perovskite	98
13	0.4389	1804.65	Barite-$BaSO_4$	23
14	0.4452	888.42	$Sc_2Si_2O_7$-Pyrochlore	23
15	0.4580	263.06	Th_2TeN_2	24

16	0.4596	2075.76	Olivine	45
17	0.4607	904.70	Tilted Perovskite	164
18	0.4765	437.28	PbCIF	39
19	0.4789	764.27	Quaternary Double Perovskite	51
20	0.4911	1877.17	Monazite	20
21	0.4918	1533.28	$CaFe_2O_4$	33
22	0.4924	1628.19	$BaCuY_2O_5$	31
23	0.4932	607.83	Double Perovskite	99
24	0.5010	257.52	Fluorite-CaF_2	24
25	0.5049	420.40	Bi_2ErO_4I	40
26	0.5162	204.74	Rocksalt	35
27	0.5223	457.48	La_2O_3	48
28	0.5334	3135.65	Apatite	22
29	0.5356	363.00	K_2MgF_4	40
30	0.5447	1022.73	La_3NbO_7(OS)	27
31	0.5527	971.13	K_4CdCl_6	64
32	0.5782	2125.45	Melilite	40
33	0.5802	1577.55	K_2SO_4	41
34	0.5851	2105.74	Pyroxene-$CaMg(SiO_3)_2$	35
35	0.5948	230.76	Delafossite	45
36	0.5982	2298.27	Bixbyite-Mn_2O_3	30
37	0.6482	358.60	Sr_2NiWO_6	37
38	0.6582	517.15	Delafossite-$NaCrS_2$	28

39	0.6672	1260.54	$CuFeO_2$	21
40	0.6807	1464.94	Hexagonal Perovskite	46
41	0.6919	350.70	Elpasolite	140

Table 3.3. A ranking of 41 oxide structure types which have at least 20 members.

According to Table 3.3, there are 11 other oxide structure types that could potentially be better proton conductors than cubic perovskite. One of them is the pyrochlore crystal class, which has been studied recently[109, 110]. The calcite structure type while promising, might not be very stable in oxidizing condition. This trimmed the top 5 of the ranking to $CrVO_4$, zircon, $NaMn_7O_{12}$, $YNbO_4$(mS24), and spinel. $YNbO_4$(mS24) is a member of the rare-earth niobates, which have been also found to be a potential proton conductor[3]. On the other hand, $CrVO_4$, zircon, and $NaMn_7O_{12}$ structure types have never been studied for proton conductivity. As our screening result has shown, these 3 structure types are potentially better than as proton conductors than cubic perovskites.

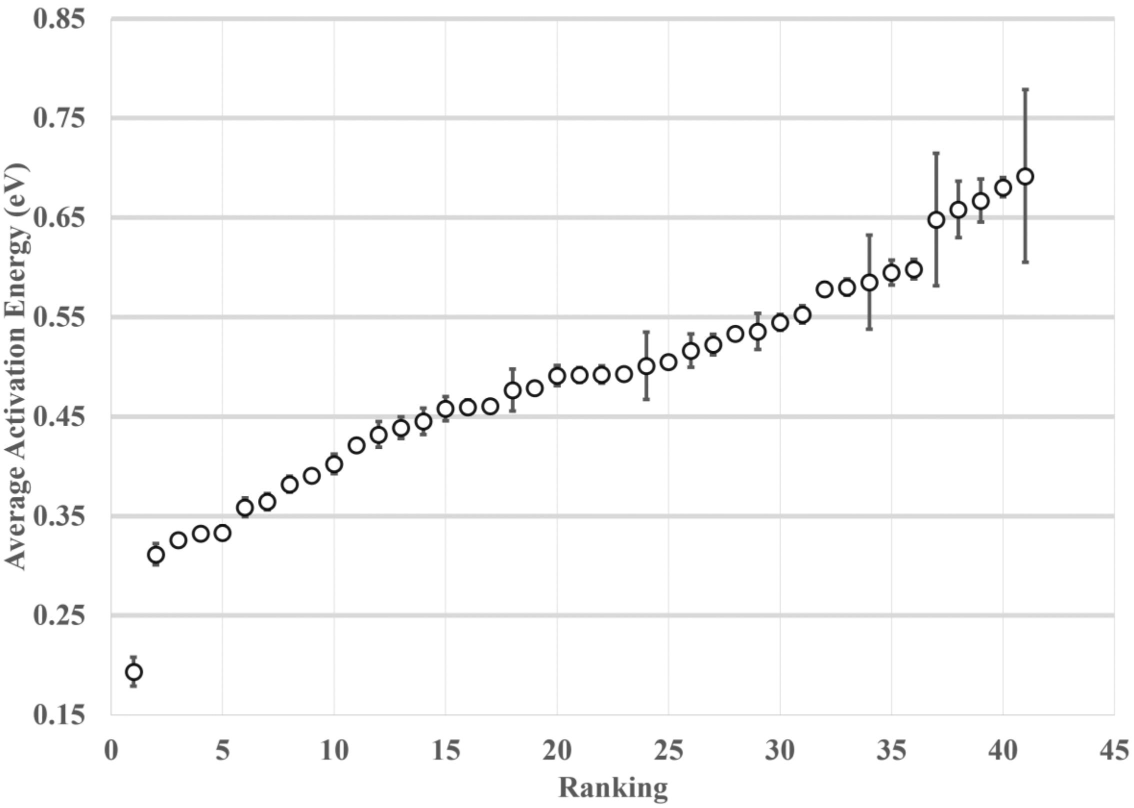

Figure 3.13 Plot of the ranking shown in Table 3.3.

We would like to note the caveat to the ranking shown in Table 3.3 through Figure 3.13. As shown in Figure 3.13, with the exception of the structure type ranked first, all other structure types are quite close with each other with respect to their average activation energy and thus not as discrete as the ranking shows. Taking into account the accuracy of activation energy approximation through the NEB method used to train the model being 0.1 eV, it would be better to think of the ranking for structure types that have average activation energy within 0.1 eV of each other to be ranked the same. This is shown inf Figure 3.13 through the y-axis gridline, where structure types within said gridline should be considered as the same rank.

$CrVO_4$ structure type that topped our ranking has an orthorhombic lattice, as shown in Figure 3.14 and is mainly studied for its magnetic properties[111, 112].

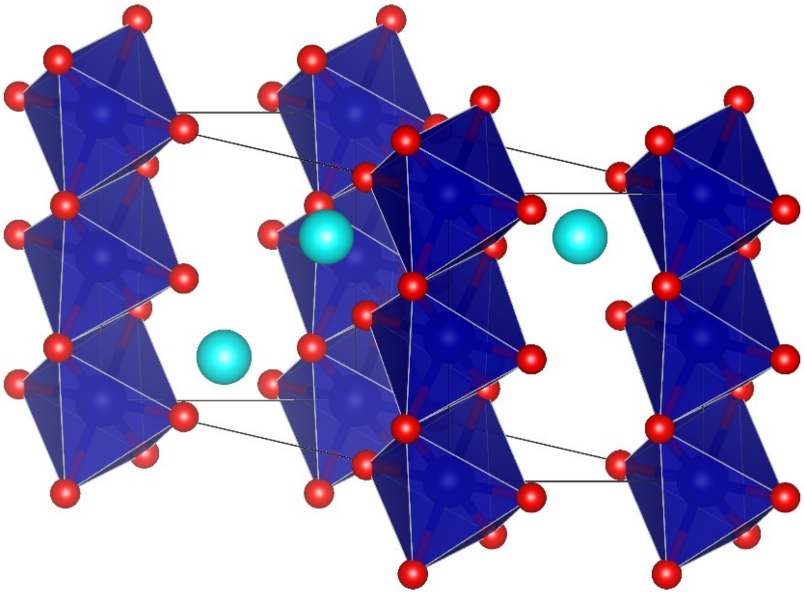

Figure 3.14 The structure of $CrVO_4$ family. Blue spheres in the tetrahedron represent chromium, aquamarine spheres represent vanadium, and small red spheres represent oxygen.

It is important to note that while on the difference between the average activation energy of $CrVO_4$ and cubic perovskite structure type is roughly 0.23 eV, the difference in proton mobility is actually quite significant. Substituting this difference into the rate equation, equation 3.1, with the temperature of 600K, which is the target temperature for PC-SOFC, we can see that the rate would be different by a factor of 85. This means that assuming the same frequency and for an operating temperature of 600K, protons in a

$CrVO_4$ structure type would on average be 85 times more mobile than on a cubic perovskite structure type.

We calculated the activation energy for proton diffusion of the $CrVO_4$ structure type using DFT+NEB in order to validate this result. The results of these calculations are shown in Table 3.4.

Composition	**Oxide Crystal Family**	**Model Predicted Activation Energy (eV)**	**DFT+NEB Calculated Activation Energy (eV)**	**Absolute Difference (eV)**
$AlPO_4$	$CrVO_4$	0.092	0.161	0.070
$TiSiO_4$	$CrVO_4$	0.049	0.091	0.042
$CoSO_4$	$CrVO_4$	0.074	0.214	0.140
$CrVO_4$	$CrVO_4$	0.272	0.172	0.100
$CrPO_4$	$CrVO_4$	0.046	0.242	0.196
PVO_4	$CrVO_4$	0.066	0.196	0.130

Table 3.4 Activation energy for six members of the $CrVO_4$ structure type member. The DFT+NEB results were calculated to validate the result from the energy model prediction.

As shown in Table 3.4, the activation energy difference between the model predicted value and DFT+NEB calculated results for each individual structure varies similar to the training results in Table 3.1. We took the average of the activation energies for both methods to minimize the noise. The average activation energy for this structure type according to DFT+NEB is 0.1794 eV, which is 0.07 eV from what was predicted by the energy model. The higher absolute energy difference can be expected as the model was not trained on this structure type. Regardless, the difference is still under the expected accuracy of activation energy approximation with the NEB method. This result is shown and contrasted with the training values in Figure 3.15.

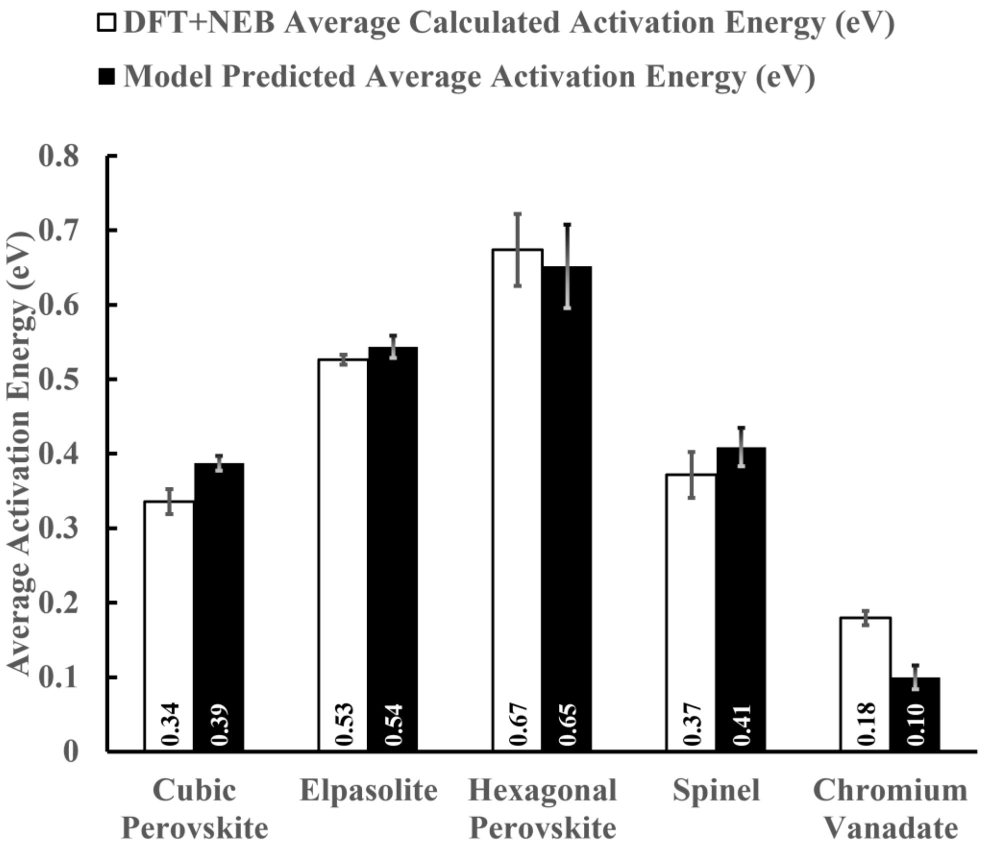

Figure 3.15 Average activation energy for DFT+NEB and the energy model with the validation $CrVO_4$ family included as a comparison.

To further validate this result, we compared the minimum energy pathway predicted by the energy model and calculated by the DFT+NEB method. As shown in Figure 3.16, the minimum energy pathway predicted by the energy model is consistent with what was calculated by the DFT+NEB method, especially the regions where the images have the highest energy, shown in red and the stables sites shown in blue. The minimum energy pathway shown in Figure 3.16 represents the minimum energy pathway of the $CrVO_4$ structure type, where the protons prefer to be near the metal with +3 oxidation state instead of the +5.

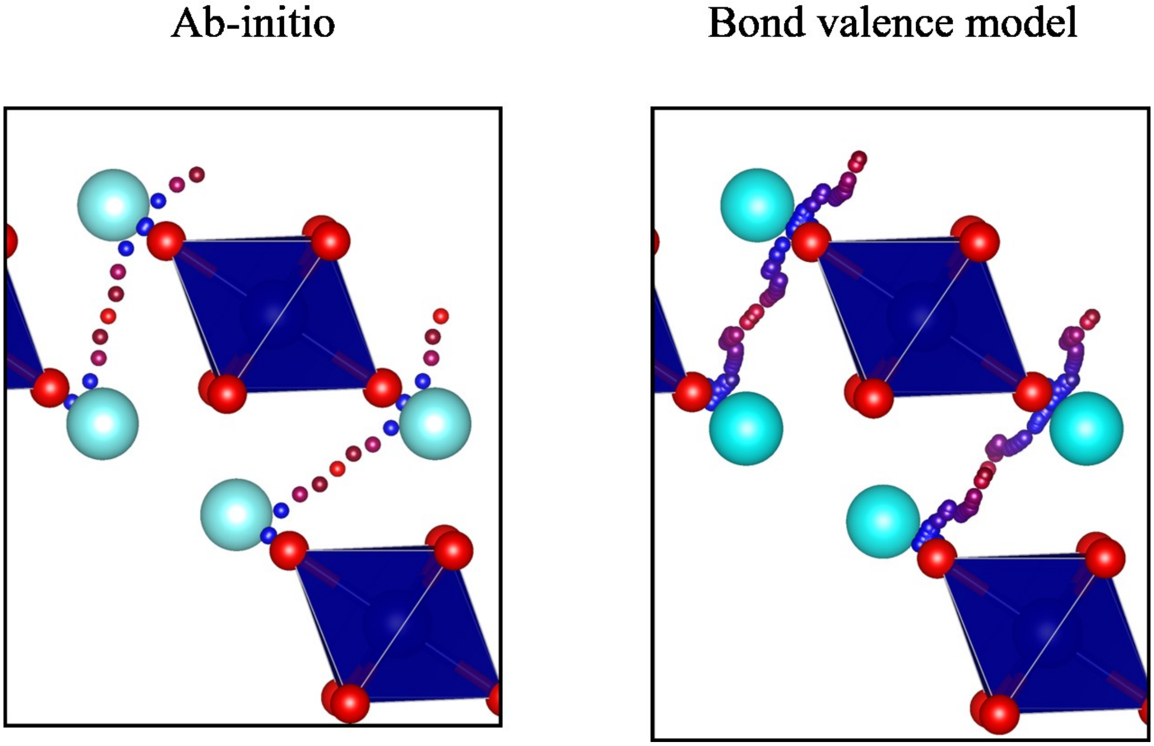

Ab-initio

Bond valence model

Figure 3.16 Fastest diffusion paths for CrVO$_4$, which is the representative of the CrVO$_4$ structure type. Aquamarine spheres represent vanadium, dark blue spheres represent magnesium, and red spheres represent oxygen. Small blue and red spheres represent the diffusion pathway, with blue indicating low energy sites and red indicating high energy sites.

3.7 Conclusion

In this chapter, we have shown that by using an energy model that consist of an exponential term backed with the BV method combined with a screening Coulomb term, we were able to rapidly screen through over 1,000 oxides. The usage of this energy model allowed us to look at the entire potential energy surface when proton is inserted of a given structure. By using the potential energy surface, we then were able to map all diffusion pathways for proton, as shown in Figure 3.9 – 3.12. Through this map, we then identified the minimum energy pathway for proton diffusion, along with its associated activation energy. This entire process on average takes less than 20 minutes in a single processor, which is a fraction of the calculation cost using DFT+NEB.

We have also shown that our energy model was able to calculate activation energy for oxide structure types within 0.1 eV. In addition, the minimum energy pathways generated by the energy model are consistent with the ones calculated by DFT+NEB.

Looking at our DFT+NEB results, we would also like to note that the spinel structure type has a real potential to compete with cubic perovskites as on average, their activation energy for proton diffusion are very close. In addition, it has been experimentally shown that hydrogen would be a proton in $MgAl_2O_4$, which is a member of this structure type [106]. However, the study for proton conductivity in this crystal class has been very rare and so we hope that this study will bring more attention to this structure type.

By using this model, we then screened the ICSD database for potential proton conducting oxides. As shown in Table 3.3, we found a number of potential oxide families which has lower activation energy than cubic perovskites, which is de facto proton conductor as of present. In addition, among those families, pyrochlores, ortho-niobate, and spinel have been shown to exhibit proton conductivity in other studies. However, the ones with the highest ranks, $CrVO_4$, zircon, and $NaMn_7O_{12}$ have not really been studied for their proton conductivities.

To validate the prediction, we did DFT+NEB calculations on 6 members of the $CrVO_4$ structure type, with the results shown in Table 3.4, Figure 3.14, and Figure 3.15. Looking at these results we can conclude that based on proton mobility, the $CrVO_4$ structure type would perform better than the cubic perovskite structure type as predicted by our model. This makes the $CrVO_4$ a possible candidate for novel proton conductors.

4. CONCLUSION AND FUTURE WORK

4.1 Efficient generation of generalized Monkhorst-Pack grids through the use of informatics

The aim of our work described in Chapter 2 is to cut down on the cost of quantum mechanical calculation. The Monkhorst-Pack grids is typically generated according to the lattice vectors of the structure in question. There were ideas on removing such constraints, but to do so requires an extensive grid search at various grid densities which is non-trivial and costly.

We approached this problem by using informatics. We began by utilizing concepts that describe the two important factors in grid selection, namely accuracy and calculation time. Accuracy is represented by the grid density whose parameter is the minimum periodic distance – the closest distance between the points in the superlattice in real space. Calculation time is represented by the number of symmetrically irreducible points, i.e. the number of times the energy equation must be solved. From here, we did extensive grid search for all existing symmetries and store the results in a database. The database can then be queried by the user within seconds. This essentially removes the costly overhead of using generalized Monkhorst-Pack grids.

To validate the efficiency of our method, we benchmarked the generalized Monkhorst-Pack grids generated using the method described in this thesis. We found that the grids we generated could make calculations go up to twice as fast. To put in in a different perspective, using these grids could cut down calculation costs by up to half.

4.1.1 Future work

To fully take advantage of the database, it is necessary to use the right minimum periodic distance value that will return a grid that is of perfect density. Typically, this is a step that is left to the user. Based on whether the material is a metal or non-metal and the size of the cell, the user will determine the value of minimum periodic distance in order to have the desired calculation accuracy. However, there are many common cases where this step become difficult to do, such as when a user is studying a new material for its properties. Alternatively, when the database is utilized to calculate many different materials (e.g. to create a database), it is impractical to figure out the ideal minimum periodic distance value. What we ended up seeing is users setting large minimum periodic distance value to ensure convergence regardless of whether the material is a metal or non-metal.

The next step to make the process more efficient, is then to leave the determination of the minimum periodic distance value to the server itself. This is a non-trivial project as it entails determining whether a material is metal or non-metal based only on its structure, i.e. guessing the bandstructure of a material. In addition, to be able to provide a minimum periodic distance value, not only the server has to determine whether a structure is metal or non-metal, it has to be able to approximate its band-gap. This significantly increases the complexity of the problem. Currently, this is being tackled by another researcher in the research group and I wish him to succeed on this.

4.2 Rapid screening for proton conductors

Proton conducting solid oxide fuel cells would be a great alternative to the currently utilized solid oxide fuel cells. PC-SOFCs have much lower operating temperature as they have proton as diffusers instead of oxygen ions. However since the discovery of proton conductivity in solids in the late 70's, proton conductors are still in the domain of laboratories[3]. Our main idea is then to use computational methods to screen through existing materials databases to find a novel structure type that could be a potential alternative in order to accelerate the development of this technology.

We began by selecting an appropriate descriptor, i.e. activation energy for proton diffusion and limited our scope to proton mobility, leaving proton solubility for future studies. In order to screen through thousands of materials within a reasonable amount of time and resources, we created an energy model. We took into account that the potential materials will be ionic and have many different combinations of elements. The BV method is well parametrized for many different elements and describe ionic materials very well. However, the BV method do not have any energy terms. To address this, we created an energy model based on this BV method using a combination of exponential repulsion term and Coulomb screening term. This energy model is very simple and contains 3 different parameters to fit, allowing it to be fit well without needing hundreds of training data.

We trained this model on activation energies obtained from NEB calculations. We found that while the model could predict the correct activation energy trend, there is a significant noise for a given structure type. To minimize this noise, we took the average activation energy for a given structure type and found that the error fell within the accuracy of the NEB calculation.

Using this model, we screened the ICSD database for potential proton conductors. We then ranked the results for structure types with at least 20 members. The ranking of the structure types is not very clear cut as the difference of average activation energy between structure types of adjacent ranks, e.g. rank 2 and 3, rank 3 and 4, is within the accuracy of the NEB calculation. It would then be best to see the ranking as groups within 0.1 eV of each other. That said, the structure type that placed first in the ranking has average activation energy that is above the accuracy of the NEB calculation and we decided to look into it further.

The structure type that placed first in the ranking was $CrVO_4$. We then calculated the activation energy for a sample of members of this structure type, i.e. $AlPO_4$, $TiSiO_4$, $CoSO_4$, $CrVO_4$, $CrPO_4$, and PVO_4. We found that the difference between the average activation energy of the value predicted by the energy model and the value calculated by the NEB calculation is 0.08 eV. This shows that $CrVO_4$ is a potential novel material for proton conductor.

4.2.2. Future work

As mentioned above, we have found $CrVO_4$ structure type as a possible novel material for proton conductors based on proton mobility. Another aspect that we did not cover in this work is hydrogen solubility in these materials. It is then a logical step to experimentally test $AlPO_4$, $TiSiO_4$, $CoSO_4$, $CrVO_4$, $CrPO_4$, and PVO_4 which we have shown computationally to have high proton mobility for their hydrogen solubility. This approach can be similar to what has been done to test cubic perovskites[113]. On top of this tests on other properties such as electrical resistivity and oxygen conductivity also need to be done in order for truly show that a material would be a great proton conductor[3].

A different and perhaps parallel approach we could also take is to study different possible dopants for these materials. Normally, studying the effect of dopants on a given material is an expensive endeavor. Depending on the position and number of dopants, they might significantly alter the diffusion process. An example of this would be the doping of scandium in $SrZrO_3$, which trap diffusing protons[114]. By using the energy model that we have developed in this thesis, one could then rapidly study different possibilities of dopant numbers, position, and combinations, allowing to truly "design" the ideal proton conductor. In the same vein, we could also study the effects of vacancies as they have been shown to also influence the behavior of diffusing protons due to the fact that a missing oxygen atom will provide extra electrons in the system[115, 116].

Finally, by having a model that is able to screen through different structure types, we can also theoretically screen solids that are not oxides, but also have anions from the VI A column, e.g. sulfides and selenides.

Bibliography

[1] Takahashi, T. and H. Iwahara, *Ionic conduction in perovskite-type oxide solid solution and its application to the solid electrolyte fuel cell.* Energy Conversion, 1971. **11**(3): p. 105-111.

[2] Iwahara, H., et al., *Proton Conduction in Sintered Oxides and Its Application to Steam Electrolysis for Hydrogen-Production.* Solid State Ionics, 1981. **3-4**(Aug): p. 359-363.

[3] Marrony, M. and P. Pan Stanford, *Proton-conducting ceramics from fundamentals to applied research*. 2016, Singapore: Pan Stanford Publishing.

[4] Singhal, S.C., *Advances in solid oxide fuel cell technology.* Solid State Ionics, 2000. **135**(1): p. 305-313.

[5] Haile, S.M., et al., *Solid acids as fuel cell electrolytes.* Nature, 2001. **410**(6831): p. 910-913.

[6] Wachsman, E.D. and K.T. Lee, *Lowering the Temperature of Solid Oxide Fuel Cells.* Science, 2011. **334**(6058): p. 935.

[7] Shao, Z., et al., *A thermally self-sustained micro solid-oxide fuel-cell stack with high power density.* Nature, 2005. **435**: p. 795.

[8] Steele, B.C.H. and A. Heinzel, *Materials for fuel-cell technologies.* Nature, 2001. **414**: p. 345.

[9] Haile, S.M., *Fuel cell materials and components☆☆☆The Golden Jubilee Issue—Selected topics in Materials Science and Engineering: Past, Present and Future, edited by S. Suresh.* Acta Materialia, 2003. **51**(19): p. 5981-6000.

[10] Mohammad, N., et al., *A review on synthesis and characterization of solid acid materials for fuel cell applications.* Journal of Power Sources, 2016. **322**: p. 77-92.

[11] G. Taillades, J.R., J. Dailly, N. Fukatsu, and R.H. A. Magrasó, and P. R. Slater, *Proton-Conducting Oxide Materials*, in *Proton-Conducting Electrolytes for Solid Oxide Fuel Cell Applications*, M. Marrony, Editor. 2016. p. 73-146.

[12] Kochetova, N., et al., *Recent activity in the development of proton-conducting oxides for high-temperature applications.* Rsc Advances, 2016. **6**(77): p. 73222-73268.

[13] Zhou, W. and Z. Shao, *Fuel cells: Hydrogen induced insulation.* Nature Energy, 2016. **1**(6): p. 16078.

[14] Zhou, Y., et al., *Strongly correlated perovskite fuel cells.* Nature, 2016. **534**(7606): p. 231-4.

[15] Kreuer, K.D., *On the development of proton conducting materials for technological applications.* Solid State Ionics, 1997. **97**(1-4): p. 1-15.

[16] Kreuer, K.D., *On the complexity of proton conduction phenomena.* Solid State Ionics, 2000. **136**: p. 149-160.

[17] Kreuer, K.D., *Proton-conducting oxides.* Annual Review of Materials Research, 2003. **33**(1): p. 333-359.

[18] Hogarth, W.H.J., J.C. Diniz da Costa, and G.Q. Lu, *Solid acid membranes for high temperature (¿140° C) proton exchange membrane fuel cells.* Journal of Power Sources, 2005. **142**(1-2): p. 223-237.

[19] Saiful Islam, M. and P.R. Slater, *Solid-State Materials for Clean Energy: Insights from Atomic-Scale Modeling.* MRS Bulletin, 2011. **34**(12): p. 935-941.

[20] Barron, O., et al., *CsHSO4 as proton conductor for high-temperature polymer electrolyte membrane fuel cells.* Journal of Applied Electrochemistry, 2014. **44**(9): p. 1037-1045.

[21] Hatada, N., et al., *Fast and Anisotropic Proton Conduction in a Crystalline Polyphosphate.* Journal of Physical Chemistry C, 2014. **118**(51): p. 29629-29635.

[22] Shimojo, F., *First-principles molecular-dynamics simulation of proton diffusion in perovskite oxides.* Solid State Ionics, 1998. **113-115**(1-2): p. 319-323.

[23] Matsushita, E. and T. Sasaki, *Theoretical approach for protonic conduction in perovskite-type oxides.* Solid State Ionics, 1999. **125**(1-4): p. 31-37.

[24] Matsushita, E. and H. Nishikawa, *Analogy between proton and lithium-ion diffusion in perovskite-type oxides.* Ferroelectrics, 2004. **301**(1): p. 101-105.

[25] Bork, N., et al., *Simple descriptors for proton-conducting perovskites from density functional theory.* Physical Review B, 2010. **82**(1): p. 014103.

[26] Munch, W., et al., *Proton diffusion in perovskites: comparison between BaCeO3, BaZrO3, SrTiO3, and CaTiO3 using quantum molecular dynamics.* Solid State Ionics, 2000. **136**: p. 183-189.

[27] Zhang, Q., et al., *Path integral treatment of proton transport processes in BaZrO3.* Phys Rev Lett, 2008. **101**(21): p. 215902.

[28] Gomez, M.A. and F.J. Liu, *Protons in Al doped BaZrO3 escape dopant traps to access long range proton conduction highways.* Solid State Ionics, 2013. **252**: p. 40-47.

[29] Dawson, J.A. and I. Tanaka, *Proton trapping in Y and Sn Co-doped BaZrO3.* Journal of Materials Chemistry A, 2015. **3**(18): p. 10045-10051.

[30] Haugsrud, R. and T. Norby, *Proton conduction in rare-earth ortho-niobates and ortho-tantalates.* Nature Materials, 2006. **5**(3): p. 193-196.

[31] Curtarolo, S., et al., *The high-throughput highway to computational materials design.* Nat Mater, 2013. **12**(3): p. 191-201.

[32] Wadia, C., A.P. Alivisatos, and D.M. Kammen, *Materials Availability Expands the Opportunity for Large-Scale Photovoltaics Deployment.* Environmental Science & Technology, 2009. **43**(6): p. 2072-2077.

[33] Lin, L.-C., et al., *In silico screening of carbon-capture materials.* Nature Materials, 2012. **11**: p. 633.

[34] Roy, A., et al., *Half-Heusler Semiconductors as Piezoelectrics.* Physical Review Letters, 2012. **109**(3): p. 037602.

[35] Greeley, J., et al., *Computational high-throughput screening of electrocatalytic materials for hydrogen evolution.* Nature Materials, 2006. **5**: p. 909.

[36] Ceder, G., *Opportunities and challenges for first-principles materials design and applications to Li battery materials.* MRS Bulletin, 2010. **35**(9): p. 693-701.

[37] Xiao, R., H. Li, and L. Chen, *High-throughput design and optimization of fast lithium ion conductors by the combination of bond-valence method and density functional theory.* Sci Rep, 2015. **5**: p. 14227.

[38] [cited 2019 Jan 16, 2019]; Available from: https://www.top500.org/statistics/perfdevel/.

[39] Eyring, H., *The activated complex in chemical reactions.* Journal of Chemical Physics, 1935. **3**(2): p. 107-115.

[40] Vineyard, G.H., *Frequency Factors and Isotope Effects in Solid State Rate Processes.* Journal of Physics and Chemistry of Solids, 1957. **3**(1-2): p. 121-127.

[41] Hohenberg, P. and W. Kohn, *Inhomogeneous Electron Gas.* Physical Review B, 1964. **136**(3b): p. B864-+.

[42] Kohn, W. and L.J. Sham, *Self-Consistent Equations Including Exchange and Correlation Effects.* Physical Review, 1965. **140**(4a): p. 1133-&.

[43] Henkelman, G. and H. Jonsson, *Improved tangent estimate in the nudged elastic band method for finding minimum energy paths and saddle points.* Journal of Chemical Physics, 2000. **113**(22): p. 9978-9985.

[44] Sheppard, D., R. Terrell, and G. Henkelman, *Optimization methods for finding minimum energy paths.* J Chem Phys, 2008. **128**(13): p. 134106.

[45] Sheppard, D. and G. Henkelman, *Paths to which the nudged elastic band converges.* J Comput Chem, 2011. **32**(8): p. 1769-71; author reply 1772-3.

[46] Sheppard, D., et al., *A generalized solid-state nudged elastic band method.* J Chem Phys, 2012. **136**(7): p. 074103.

[47] Pauling, L., *The principles determining the structure of complex ionic crystals.* Journal of the American Chemical Society, 1929. **51**(1-4): p. 1010-1026.

[48] Brown, I.D. and R.D. Shannon, *Empirical bond-strength–bond-length curves for oxides.* Acta Crystallographica Section A, 1973. **29**(3): p. 266-282.

[49] Altermatt, D. and I.D. Brown, *The Automatic Searching for Chemical-Bonds in Inorganic Crystal-Structures.* Acta Crystallographica Section B-Structural Science, 1985. **41**(Aug): p. 240-244.

[50] Bragg, W.L., *XXV. The Structure of Silicates*, in *Zeitschrift für Kristallographie - Crystalline Materials*. 1930. p. 237.

[51] Brown, I.D., *Recent developments in the methods and applications of the bond valence model.* Chem Rev, 2009. **109**(12): p. 6858-919.

[52] Adams, S. and J. Swenson, *Migration pathways in Ag-based superionic glasses and crystals investigated by the bond valence method.* Physical Review B, 2000. **63**(5).

[53] Van der Ven, A., J. Bhattacharya, and A.A. Belak, *Understanding Li diffusion in Li-intercalation compounds.* Acc Chem Res, 2013. **46**(5): p. 1216-25.

[54] Wang, Y., et al., *Design principles for solid-state lithium superionic conductors.* Nat Mater, 2015. **14**(10): p. 1026-31.

[55] Adams, S. and J. Swenson, *Bond valence analysis of transport pathways in RMC models of fast ion conducting glasses.* Physical Chemistry Chemical Physics, 2002. **4**(14): p. 3179-3184.

[56] Adams, S., *From bond valence maps to energy landscapes for mobile ions in ion-conducting solids.* Solid State Ionics, 2006. **177**(19-25): p. 1625-1630.

[57] Baldereschi, A., *Mean-Value Point in the Brillouin Zone.* Physical Review B, 1973. **7**(12): p. 5212-5215.

[58] Chadi, D.J. and M.L. Cohen, *Special Points in the Brillouin Zone.* Physical Review B, 1973. **8**(12): p. 5747-5753.

[59] Monkhorst, H.J. and J.D. Pack, *Special Points for Brillouin-Zone Integrations.* Physical Review B, 1976. **13**(12): p. 5188-5192.

[60] Froyen, S., *Brillouin-zone integration by Fourier quadrature: Special points for superlattice and supercell calculations.* Phys Rev B Condens Matter, 1989. **39**(5): p. 3168-3172.

[61] Moreno, J. and J.M. Soler, *Optimal meshes for integrals in real- and reciprocal-space unit cells.* Phys Rev B Condens Matter, 1992. **45**(24): p. 13891-13898.

[62] José, M.S., et al., *The SIESTA method for ab initio order- N materials simulation.* Journal of Physics: Condensed Matter, 2002. **14**(11): p. 2745.

[63] Wisesa, P., K.A. McGill, and T. Mueller, *Efficient generation of generalized Monkhorst-Pack grids through the use of informatics.* Physical Review B, 2016. **93**(15): p. 155109.

[64] Sholl, D., J.A. Steckel, and Sholl, *Density Functional Theory : a Practical Introduction*. 2011, Somerset: Wiley.

[65] Kresse, G. and J. Hafner, *Ab initio molecular dynamics for liquid metals.* Phys Rev B Condens Matter, 1993. **47**(1): p. 558-561.

[66] Kresse, G. and J. Hafner, *Ab initio molecular-dynamics simulation of the liquid-metal-amorphous-semiconductor transition in germanium.* Phys Rev B Condens Matter, 1994. **49**(20): p. 14251-14269.

[67] Kresse, G. and J. Furthmuller, *Efficient iterative schemes for ab initio total-energy calculations using a plane-wave basis set.* Physical Review B, 1996. **54**(16): p. 11169-11186.

[68] Kresse, G. and J. Furthmuller, *Efficiency of ab-initio total energy calculations for metals and semiconductors using a plane-wave basis set.* Computational Materials Science, 1996. **6**(1): p. 15-50.

[69] Kresse, G. and D. Joubert, *From ultrasoft pseudopotentials to the projector augmented-wave method.* Physical Review B, 1999. **59**(3): p. 1758-1775.

[70] Aroyo, M.I. and H. Wondratschek, in *International Tables for Crystallography*. 2006, John Wiley & Sons, Ltd.

[71] Nguyen, P.Q. and D. Stehlé, *Low-dimensional lattice basis reduction revisited.* ACM Transactions on Algorithms, 2009. **5**(4): p. 1-48.

[72] Semaev, I. *Cryptography and lattices : International Conference, CaLC 2001, Providence, RI, USA, March 29-30, 2001, revised papers*. Berlin: Springer.

[73] *Inorganic Crystal Structure Database*. Available from: http://www.fiz-karlsruhe.de/icsd.html.

[74] Blochl, P.E., *Projector Augmented-Wave Method.* Physical Review B, 1994. **50**(24): p. 17953-17979.

[75] Blochl, P.E., O. Jepsen, and O.K. Andersen, *Improved Tetrahedron Method for Brillouin-Zone Integrations.* Physical Review B, 1994. **49**(23): p. 16223-16233.

[76] He, L. and D. Vanderbilt, *Exponential decay properties of Wannier functions and related quantities.* Phys Rev Lett, 2001. **86**(23): p. 5341-4.

[77] Ismail-Beigi, S. and T.A. Arias, *Locality of the density matrix in metals, semiconductors, and insulators.* Physical Review Letters, 1999. **82**(10): p. 2127-2130.

[78] Taraskin, S.N., D.A. Drabold, and S.R. Elliott, *Spatial decay of the single-particle density matrix in insulators: analytic results in two and three dimensions.* Phys Rev Lett, 2002. **88**(19): p. 196405.

[79] Jain, A., et al., *Commentary: The Materials Project: A materials genome approach to accelerating materials innovation.* Apl Materials, 2013. **1**(1): p. 011002.

[80] Curtarolo, S., et al., *AFLOWLIB.ORG: A distributed materials properties repository from high-throughput ab initio calculations.* Computational Materials Science, 2012. **58**: p. 227-235.

[81] Saal, J.E., et al., *Materials Design and Discovery with High-Throughput Density Functional Theory: The Open Quantum Materials Database (OQMD).* Jom, 2013. **65**(11): p. 1501-1509.

[82] *TOMCAT*. 2019; Available from: http://tomcat.apache.org/.

[83] *Apache Commons*. Available from: https://commons.apache.org/

[84] Giannozzi, P., et al., *QUANTUM ESPRESSO: a modular and open-source software project for quantum simulations of materials.* J Phys Condens Matter, 2009. **21**(39): p. 395502.

[85] Giannozzi, P., et al., *Advanced capabilities for materials modelling with Q uantum ESPRESSO.* Journal of Physics: Condensed Matter, 2017. **29**(46): p. 465901.

[86] Gonze, X., et al., *First-principles computation of material properties: the ABINIT software project.* Computational Materials Science, 2002. **25**(3): p. 478-492.

[87] Bryan, G.S., *Edison, the man and his work*. 2010.

[88] Shimojo, F., K. Hoshino, and H. Okazaki, *First-principles molecular-dynamics simulation of proton diffusion in Sc-doped SrTiO3.* Journal of the Physical Society of Japan, 1997. **66**(1): p. 8-10.

[89] Hafner, J., C. Wolverton, and G. Ceder, *Toward computational materials design: The impact of density functional theory on materials research.* Mrs Bulletin, 2006. **31**(9): p. 659-665.

[90] Shi, C. and M. Morinaga, *Doping effects on proton incorporation and conduction in SrZrO3.* J Comput Chem, 2006. **27**(6): p. 711-8.

[91] Gomez, M.A., et al., *Comparison of proton conduction in KTaO3 and SrZrO3.* J Chem Phys, 2007. **126**(19): p. 194701.

[92] Sundell, P.G., M.E. Björketun, and G. Wahnström, *Density-functional calculations of prefactors and activation energies for H diffusion inBaZrO3.* Physical Review B, 2007. **76**(9): p. 094301.

[93] Bork, N., et al., *Thermodynamic and kinetic properties of hydrogen defect pairs in SrTiO3 from density functional theory.* Phys Chem Chem Phys, 2011. **13**(33): p. 15256-63.

[94] Lin, H., et al., *Non-Grotthuss proton diffusion mechanism in tungsten oxide dihydrate from first-principles calculations.* Journal of Materials Chemistry A, 2014. **2**(31): p. 12280-12288.

[95] Dawson, J.A., H. Chen, and I. Tanaka, *Protonic defects in yttria stabilized zirconia: incorporation, trapping and migration.* Phys Chem Chem Phys, 2014. **16**(10): p. 4814-22.

[96] Kato, K., et al., *Proton Channels along Oxygen Octahedral Chains in La3NbO7.* Journal of Physical Chemistry C, 2014. **118**(18): p. 9377-9384.

[97] Henkelman, G., *Methods for Calculating Rates of Transitions with Application to Catalysis and Crystal Growth*, in *Chemistry*. 2001, University of Washington. p. 157.

[98] Henkelman, G., B.P. Uberuaga, and H. Jonsson, *A climbing image nudged elastic band method for finding saddle points and minimum energy paths.* Journal of Chemical Physics, 2000. **113**(22): p. 9901-9904.

[99] O'Keefe, M. and N.E. Brese, *Atom sizes and bond lengths in molecules and crystals.* Journal of the American Chemical Society, 1991. **113**(9): p. 3226-3229.

[100] Muller, O. and R. Roy, *The major ternary structural families*. 1974, New York: Springer-Verlag.

[101] Wood, D.M. and A. Zunger, *A New Method for Diagonalizing Large Matrices.* Journal of Physics a-Mathematical and General, 1985. **18**(9): p. 1343-1359.

[102] Pulay, P., *Convergence acceleration of iterative sequences. the case of scf iteration.* Chemical Physics Letters, 1980. **73**(2): p. 393-398.

[103] Perdew, J.P., K. Burke, and M. Ernzerhof, *Generalized Gradient Approximation Made Simple.* Phys Rev Lett, 1996. **77**(18): p. 3865-3868.

[104] Pauling, L., *The nature of the chemical bond IV The energy of single bonds and the relative electronegativity of atoms.* Journal of the American Chemical Society, 1932. **54**(9): p. 3570-3582.

[105] Momma, K. and F. Izumi, *VESTA 3 for three-dimensional visualization of crystal, volumetric and morphology data.* Journal of Applied Crystallography, 2011. **44**(6): p. 1272-1276.

[106] Fukatsu, N., et al., *Incorporation of hydrogen into magnesium aluminate spinel.* Solid State Ionics, 2002. **152-153**: p. 809-817.

[107] Zhao, Q., et al., *Spinels: Controlled Preparation, Oxygen Reduction/Evolution Reaction Application, and Beyond.* Chemical Reviews, 2017. **117**(15): p. 10121-10211.

[108] Creutz, S.E., et al., *Colloidal Nanocrystals of Lead-Free Double-Perovskite (Elpasolite) Semiconductors: Synthesis and Anion Exchange To Access New Materials.* Nano Letters, 2018. **18**(2): p. 1118-1123.

[109] Hatnean, M.C., et al., *Structural and magnetic investigations of single-crystalline neodymium zirconate pyrochloreNd2Zr2O7.* Physical Review B, 2015. **91**(17).

[110] Toyoura, K., A. Nakamura, and K. Matsunaga, *First-Principles Analysis of Proton Conduction Mechanism in Pyrochlore-Structured Lanthanum Zirconate.* Journal of Physical Chemistry C, 2015. **119**(16): p. 8480-8487.

[111] Frazer, B.C. and P.J. Brown, *Antiferromagnetic Structure of CrVO4and the Anhydrous Sulfates of Divalent Fe, Ni, and Co.* Physical Review, 1962. **125**(4): p. 1283-1291.

[112] Isasi, M.J., et al., *Synthesis and magnetic properties of crystalline CrVO4.* Materials Research Bulletin, 1988. **23**(4): p. 595-601.

[113] Grimaud, A., et al., *Transport properties and in-situ Raman spectroscopy study of BaCe0.9Y0.1O3−δ as a function of water partial pressures.* Solid State Ionics, 2011. **191**(1): p. 24-31.

[114] Hempelmann, R., et al., *Muon diffusion and trapping in proton conducting oxides.* Solid State Ionics, 1998. **107**(3): p. 269-280.

[115] Chen, Q., et al., *Observation of Oxygen Vacancy Filling under Water Vapor in Ceramic Proton Conductors in Situ with Ambient Pressure XPS.* Chemistry of Materials, 2013. **25**(23): p. 4690-4696.

[116] Knight, K.S., *Structural phase transitions, oxygen vacancy ordering and protonation in doped BaCeO3: results from time-of-flight neutron powder diffraction investigations.* Solid State Ionics, 2001. **145**(1): p. 275-294.

Curriculum Vitae

Pandu Wisesa was born in November 1989 in Jakarta, Indonesia. In 2008, he enrolled at Illinois Institute of Technology in Chicago before transferring to University of Illinois in 2010. In University of Illinois he did computational research on the behavior of oxygen atoms in HCP metals under Prof. Dallas Trinkle and Dr. Henry Wu. In May 2012, he received his Bachelor of Science degree from the Department of Materials Science and Engineering at University of Illinois. In the fall of 2012, he joined the Ph.D. program in the Department of Materials Science and Engineering at Johns Hopkins University under Prof. Tim Mueller. In the Mueller research group, under the guidance of Prof. Tim Mueller, he has created and maintained the *k*-point grid database, along with a publicly available server, and other assorted tools to support the server. He has also utilized an energy model to screen through a materials database and discovering structures that could potentially be novel proton conductors.